

Large Eddy Simulation of oscillatory flow over a mobile rippled bed using an Euler-Lagrange approach

Daniel Stokes Hagan

1 Abstract

A volume-filtered Large-Eddy Simulation (LES) of oscillatory flow over a rippled mobile bed is conducted using an Euler-Lagrange approach. This work is done to complement the experimental work of Frank et. al. [26], which shows quasi-steady state ripples in a sand bed under oscillatory flow, as observed in unsteady marine flows over sedimentary beds. This work approximates the experimental configuration with a sinusoidal pressure gradient driven flow and a sinusoidally shaped rippled bed of particles. The LES equations, which are volume-filtered to account for the effect of the particles, are solved on an Eulerian grid, and the particles are tracked in a Lagrangian framework. A Discrete Particle Method (DPM) is used in this work, where the particle collisions are handled by a soft-sphere model, and the liquid and solid phases are coupled through volume fraction and momentum exchange terms. Comparison of the numerical results to the experimental data show that the LES-DPM is capable of capturing the mesoscale features of the system. The large scale shedding of vortices from the ripple peaks are observed in both datasets, which is reflected in the good quantitative agreement between the wall-normal flow statistics, and good qualitative agreement in ripple shape evolution and sand grain/particle entrainment behavior above the fluid-bed interface. Additionally, the numerical data provide some insight into the complex dynamics between the solid and fluid phases. First, in addition to short-term suspended load (particle entrainment/saltation), a transport layer of mobile interface particles, or bedload, is observed, which helps to maintain the ripple structure. Second, the interaction between coherent fluid structures formed at adjacent ripples are heavily three-dimensional, resulting in particle motion that is not spatially or temporally uniform.

2 Introduction

2.1 Numerical Methods

Until recently, numerical studies of scour and ripple formation, and their effects on flow characteristics, have traditionally treated the sediment bed as a continuum. The bed load, and if represented, the suspended load, are treated as scalar concentrations. The morphology of the sediment bed is governed by a bed load transport equation and the suspended load is governed by the convection-diffusion transport equation. An alternative numerical approach to the bed load transport method is the Discrete Particle Method (DPM), which is used in this work. The DPM treats the fluid as a continuum and the particles as distinct entities. The model is four-way coupled, whereby the fluid feels the effects of each particle, each particle feels the effect of the surrounding fluid, and each particle can feel the effect of any other particle. The model was pioneered by Cundall and Strack [16], and has many applications in particle-fluid flows. The details of the model are summarized in Section 3, following the application by Pepiot and Desjardins [39]. For full reviews of the theoretical developments of the method, and applications, see Zhu et al. [53, 54] and Deen et al. [17], respectively.

The majority of the implementations of the bed load approach are often paired with either Reynolds Averaged Navier-Stokes (RANS) simulations or Large Eddy Simulation (LES) to

model flow. It is important to note that these methods model all (RANS) or small-scale (LES) flow structures, and must rely on turbulence models for non-laminar flows. By design, RANS solvers use time-averaged equations. Flow variables are decomposed into two components, the time-averaged value, and the fluctuation. Therefore, RANS solvers cannot accurately predict strongly time-dependent phenomena, like the oscillatory flow over a rippled bed presented in this work. LES applies the flow variables through a low-pass filter, removing the high-frequency, or small-scale, structures. The low-frequency components, or large scales, of the flow are fully resolved directly, but the small scales are modeled in order to reduce computational cost. Since sediment scour occurs at the interface between the fluid and the sediment bed, exactly where the smallest scales of the flow are observed, LES may be filtering out flow characteristics that are crucial to scouring processes. By contrast, Direct Numerical Simulation (DNS) fully resolves all scales of the flow, but can be exponentially more demanding computationally. However, the literature has shown LES to be a good compromise between fidelity and computational feasibility. The capability of LES to describe the mesoscale features of the flow will be shown in this work.

2.2 Oscillatory Flow

Oscillatory flow is generally driven by a sinusoidal pressure gradient, to which the freestream velocity is directly correspondent. In the presence of a no-slip wall, a point of inversion is observed in which the velocity near the wall is slower to respond to the reversing pressure gradient than the freestream velocity. Within a single oscillation period, four regimes of oscillatory flow have been identified by Akhavan et al. [1] using DNS. The regimes are laminar, disturbed laminar (during acceleration), intermittently turbulent (during deceleration), and fully turbulent. Di Liberto and Ciofalo [20] ran DNS of oscillatory flow in a plane channel, and were able to confirm the four flow regimes identified by Akhavan et al. [1]. The experimental work of Hino et al. [32] on transition to turbulence showed that the critical Reynolds number for transition decreases with increasing frequency of oscillation. Hino et al. [31] also noted the suppression of turbulence in the acceleration phase and the explosive and violent bursting motion at the beginning of the deceleration phase. Scotti and Piomelli [43] conducted DNS and LES of an oscillating turbulent channel. In comparing to the DNS and experimental data, the validity of the LES for purely oscillatory flow was demonstrated. For a full review of the literature on pulsatile/oscillatory flow theory, see Gundogdu and Carpinlioglu [29] [30], which focuses on classifications and relevant experimental and theoretical work of the time.

2.3 Oscillatory Flow & Bedforms

The study of oscillatory flow over rippled bedforms goes back to the seminal experimental work of Bagnold [3], in which a section of a sandy bed was oscillated through still water, focusing on “vortex ripples” as opposed to “rolling grain” ripples. “Vortex ripples” are defined to have a much larger ripple amplitude to ripple wavelength ratio than rolling grain ripples. And, therefore, the ripples can act as bluff bodies off of which vortices can be shed. In the presence of a mobile bed, Benjamin [4] determined the lag between the pressure gradient and velocity to play a central role in ripple formation. Blondeaux [6] and Vittori and Blondeaux [48] used linear, and weakly nonlinear, stability analyses to create a predictive model of sand ripple formation, and their time development, under sea waves. But, as noted by Charru and Hinch [13], the lack of growth rate measurements, fundamental to testing stability theories, is problematic. Charru and Hinch [12] also proposed a method to predict ripple formation by treating the sediment bed as a scalar and using a conservation equation which contains erosion-rate and deposition-rate terms. The authors introduced a stabilizing term to account for the phenomena that ripples do not grow when the fluid viscosity is increased, which is a departure from the Exner approach [38], which places an algebraic dependence of the particle flux on the bed shear

stress. In the second part of their study of ripple formation, the authors find that ripples can form in oscillating flow at flow velocities lower than that required in unidirectional flows. Despite neglecting the interaction between entrained sediment and the flow, the results compare favorably to experimental results in the literature. The works of Engelund and Fredsøe [22], Charru et al. [11], Best [5], and Church [15] provide comprehensive reviews of bed formations and fluid dynamics of mostly unidirectional flow systems.

In place of truly mobile beds, a variety of methods have been used to simulate their effect. Vittori and Verzicco [49] performed numerical simulations of oscillatory flow over a wavy wall, confirming that imperfections of the boundary are fundamental to the production of disturbances associated with turbulence. Fornarelli and Vittori [23] used DNS and an immersed boundary technique to simulate oscillatory flow over a rough wall, composed of fixed spherical particles. In a similar manner to Fornarelli and Vittori [23], Ghodke and Apte [28] examined the effects of wall roughness on an oscillatory flow using a DNS and immersed boundary method to model the wall roughness with fully resolved fixed particles. The highly resolved simulations show that the velocity and pressure fluctuations are non-Gaussian in their distribution. Mazzuoli et al. [36] performed fully resolved DNS-IB simulations of particle chain formation under an oscillatory flow. The simulations were performed on a smooth wall and a rough wall, composed of fixed particles. Even when the particles were initially aligned in chains in the streamwise direction, the oscillating flow caused the particles to realign into chains in the spanwise direction, which supports Yalin's [50] conclusion that bedforms are statistically two-dimensional in the spanwise direction.

Sun and Xiao [45] demonstrated that modeling particles by volume-filtering the Navier-Stokes equations is able to capture the essential features of sediment transport at a fraction of the computational cost of fully resolving individual particles, as with immersed boundary techniques. Schmeeckle [42] used LES and momentum exchange between the particles and the fluid to show that saltation is not a good model for sediment transport in unidirectional flow. Instead, bed load, also known as surface creep or reptation, and entrainment, by turbulent structures called sweeps, are the main modes of sediment transport under higher Reynolds number unidirectional flows.

Using volume-filtered Euler-Lagrange LES, Capecelatro and Desjardins [7] built a framework in which simulations are four-way coupled, allowing for particle-particle soft sphere contact, particle-fluid, and fluid-particle interactions. Arolla and Desjardins [2] utilized this methodology to model the liquid-slurry flow of particles at the bottom of a turbulent pipe. The evolution of the liquid-bed interface is characterized through the statistical analysis of the flow velocity, particle concentration, and other parameters. The flow is resolved on a grid that is of the same order as the particle diameter, as in the simulation that is the focus of this work. Capecelatro and Desjardins [9], while still coupling the particles with other particles and the fluid, showed the validity of this method for predicting bedforms. In the form of a code called NGA, these works all utilize the numerical methodology described in Desjardins et al. [19]. NGA was also used for the simulations shown in this work. Therefore, the methodology is described in more detail in the Numerical Methodology Section 3.

Although limited, some numerical work has been conducted in which the solid phase is fully resolved. Derkens [18] conducted fully resolved DNS-IB simulations of the erosion of a granular bed by turbulent flow. Simulations were conducted over a range of Shields numbers, but bedforms were not captured due to the limited nature of the domain, which was only 45 particle diameters. Kidanemariam and Uhlmann [33] have conducted a fully resolved DNS of flow over a mobile sediment bed. The sediment particles are each individually resolved using an immersed boundary technique, and the simulations are four-way coupled, with particle-particle interactions using a soft-sphere contact model. The emergence of smaller dunes and larger "vortex" dunes were observed, and the wavelength, amplitude, and celerity of the emergent dunes were found to be in good agreement with experimental data. However, as

the authors note, fully resolving all scales of the flow and sediment bed has a computational cost, and some goals are still a challenge, such as limits to domain size and simulation running time. Kidanemariam and Uhlmann [34] continue by extending the computational domain, but otherwise using the same configuration as their previous work [33]. The minimum domain length that accommodated bed deformation showed pattern formation in the range of 75-100 particle diameters. In a much longer domain, the range is 100-110 particle diameters. Two regimes of pattern growth were identified. The initial growth regime is exponential and independent of the domain length. The second is nonlinear and strongly constrained by the domain length. The authors note that, for smaller domains, the second regime is steady, demonstrating a wavelength equal to the domain length.

2.4 Motivation

The work presented here is designed to capture the mesoscale features of both the fluid and solid phases, while maintaining computational feasibility. Utilizing LES, the fluid is resolved at almost all scales, except the smallest, which are modeled. This approach is paired with a DPM in which particles are individually modeled by volume-averaging the governing equations of the flow, and particle-particle interactions are controlled by a soft-sphere collision model. In general, this approach has shown good fidelity to experimental mixed-phase flows. And, specifically, the NGA code used here has demonstrated it's applicability to unidirectional ripple formation in pipe flow. As will be shown, application of the LES-DPM approach to the flow configuration in this work shows good agreement with experimental results and provides some insight into the three-dimensional nature of the fluid-bed interaction.

3 Governing Equations & Numerical Methodology

The gas/fluid phase is governed by the Low Mach Approximation incompressible Navier-Stokes equations, and the solid phase particles are described by the Discrete Particle Method (DPM), or Lagrangian Particle Tracking (LPT) method, as described by Capecelatro and Desjardins [8] and Pepiot and Desjardins [39]. These equations are implemented in an arbitrarily high-order, massively parallel numerical code capable of direct numerical simulations (DNS), described by Desjardins et al. [19]. However, in this work, a Large Eddy Simulation (LES) was conducted. Using the same methodology as Arolla and Desjardins [2], the large scales of the flow are resolved, but the smaller scales are modeled at the sub-grid scale (SGS).

This code is staggered in both space and time, and, in this work, spatial and temporal integrations are second-order accurate. The scheme conserves mass, momentum, and energy. Time advancement is done using a fractional step Crank-Nicolson scheme. A second-order Runge-Kutta scheme is employed to solve for the position, velocity, and angular velocity of each particle. The coupling between the fluid and solid phases is achieved through the volume fraction and interphase forcing terms, which is discussed in the following sections. For the full details, the reader is referred to Desjardins et al. [19] and Pepiot and Desjardins [39]. The following serves as an overview of their methodology found in Arolla and Desjardins [2], in which this methodology was shown to satisfactorily predict ripple formations under directional pipe flow.

The Navier-Stokes equations take into account the volume occupied by the particles by volume-filtering over the Eulerian grid. Therefore, the continuity equation is

$$\frac{\partial}{\partial t} (\psi_f \rho_f) + \nabla \cdot (\psi_f \rho_f \mathbf{u}_f) = 0, \quad (1)$$

where ψ_f is the volume fraction of the fluid, ρ_f is the density of the fluid, and \mathbf{u}_f is the velocity of the fluid. With the addition of a source term for the exchange of momentum with the solid

phase, \mathbf{F}_{inter} , the conservation of momentum equation becomes

$$\frac{\partial}{\partial t} (\psi_f \rho_f \mathbf{u}_f) + \nabla \cdot (\psi_f \rho_f \mathbf{u}_f \mathbf{u}_f) = \nabla \cdot (\boldsymbol{\tau} - \mathbf{R}) + \mathbf{F}_{pgrad} + \mathbf{F}_{gravity} - \mathbf{F}_{inter}. \quad (2)$$

$\mathbf{F}_{pgrad} = \mathbf{p}_{x,0} \cos(\omega t)$ is the oscillating pressure gradient driving the flow. The gravity force is $\mathbf{F}_{gravity} = \psi_f \rho_f \mathbf{g}$. \mathbf{R} is the unresolved sub-grid stress that results from spatially filtering the velocity field, and $\boldsymbol{\tau}$ is the stress tensor

$$\boldsymbol{\tau} = -p \mathbf{I} + \boldsymbol{\sigma} + \mathbf{R}. \quad (3)$$

The pressure is denoted by p and the viscous stress tensor, $\boldsymbol{\sigma}$ is defined as

$$\boldsymbol{\sigma} = \mu (\nabla \mathbf{u}_f + \nabla \mathbf{u}_f^T) - \frac{2}{3} \mu \nabla \cdot \mathbf{u}_f \mathbf{I}, \quad (4)$$

where μ is the dynamic viscosity. The isotropic part of \mathbf{R} is absorbed into pressure, and the anisotropic part of \mathbf{R} is

$$\mathbf{R} - \frac{1}{3} \text{trace}(\mathbf{R}) \simeq \mu_t (\nabla \mathbf{u}_f + \nabla \mathbf{u}_f^T). \quad (5)$$

The turbulent viscosity, μ_t , is dynamically calculated by a Smagorinsky model [44] [27] [35] in conjunction with the Lagrangian averaging of Meneveau [37]. Since the flow is complex, Meneveau's method follows a parcel of fluid in a Lagrangian framework and uses its history to determine the μ_t .

The solid phase particles are tracked in a Lagrangian framework, where the location of an individual particle is defined by

$$\frac{d\mathbf{x}_p}{dt} = \mathbf{u}_p. \quad (6)$$

According to Newton's second law of motion, particles are governed by

$$m_p \frac{d}{dt} (\mathbf{u}_p) = \mathbf{f}_{inter} + \mathbf{F}_{col} + m_p \mathbf{g}, \quad (7)$$

where m_p is the mass of the particle, \mathbf{u}_p is the velocity of the particle, \mathbf{f}_{inter} is the exchange of momentum with the fluid for the single particle, and \mathbf{F}_{col} is the force imparted by collisions with other particles or a wall. Since the particles are assumed to be perfect spheres, the particle mass is a function of particle density, ρ_p , and particle diameter, d ,

$$m_p = \frac{\rho_p \pi d^3}{6}. \quad (8)$$

For a given cell volume, the sum of all of the N_p -total individual particle momentum exchanges, \mathbf{f}_{inter}^i , gives the full momentum exchange term in Equation 2

$$\mathbf{F}_{inter} = \sum_i^{N_p} \mathbf{f}_{inter}^i. \quad (9)$$

The collision term, \mathbf{F}_{col} , represents the sum of the all collision forces acting on a given particle.

The force that the surrounding fluid exerts on an isolated particle is

$$\mathbf{f}_{inter} = V_p \nabla \cdot \boldsymbol{\tau} + \mathbf{f}_{drag}. \quad (10)$$

The drag force is formulated as

$$\mathbf{f}_{drag} = \frac{18 m_p \mu \psi_f}{\rho_p d_p^2} (\mathbf{u}_f - \mathbf{u}_p) F(\psi_f, Re_p). \quad (11)$$

The function F is the formulation of Tenneti et al. [46] formulation for a dimensionless drag coefficient, which relies solely on the volume fraction of the fluid and the Reynolds number of the particle.

The soft-sphere model of Cundall and Strack [16] is used to determine the particle-particle collision forces. The normal component of a collision is described by a spring-dashpot model. For any two particles a and b , d_{ab} is the distance between the centers, and r_i is the radius of any particle i . A collision spring force is generated if $d_{ab} < (r_a + r_b + \lambda_{col})$, otherwise, the collision force is zero. The λ_{col} buffer region increases the stability of the algorithm because particle overlap is not required for collision. Therefore, on average, colliding particles do not overlap. Thus the normal component of collision force generated by particle a acting on particle b is

$$\mathbf{f}_{col}^{n,a \rightarrow b} = k\delta\mathbf{n}_{ab} - \eta\mathbf{u}_{n,ab}, \quad (12)$$

where k is the spring constant, η is the dashpot damping coefficient, δ is the particle overlap, \mathbf{n}_{ab} is the unit normal vector between the centers of particles a and b , and $\mathbf{u}_{n,ab}$ is the normal relative velocity between particles a and b defined as

$$\mathbf{u}_{n,ab} = ((\mathbf{u}_a - \mathbf{u}_b) \cdot \mathbf{n}_{ab})\mathbf{n}_{ab}. \quad (13)$$

The damping coefficient is written

$$\eta = -2\ln e \frac{\sqrt{m_{ab}k}}{\sqrt{\pi^2 + (\ln e)^2}}, \quad \text{with} \quad m_{ab} = \frac{m_a m_b}{m_a + m_b}, \quad (14)$$

where the restitution coefficient is $0 < e < 1$ and the mass of any particle i is m_i .

As a result of inter-particle friction, particles can obtain angular velocities due to tangential collisions. The tangential force generated when particle a acts on particle b is

$$\mathbf{f}_{col}^{t,a \rightarrow b} = \begin{cases} -k_t\delta_t - \eta_t\mathbf{u}_{t,ab}, & \text{if } |\mathbf{f}_{col}^{t,a \rightarrow b}| \leq \mu_f |\mathbf{f}_{col}^{n,a \rightarrow b}| \\ -\mu_f |\mathbf{f}_{col}^{n,a \rightarrow b}| \mathbf{t}_{ab}, & \text{if } |\mathbf{f}_{col}^{t,a \rightarrow b}| > \mu_f |\mathbf{f}_{col}^{n,a \rightarrow b}|, \end{cases} \quad (15)$$

where k_t is the tangential spring stiffness, δ_t is the tangential displacement, η_t tangential damping coefficient, μ_f is the friction coefficient, and $\mathbf{u}_{t,ab}$ is the relative tangential velocity defined as

$$\mathbf{u}_{t,ab} = \mathbf{u}_{ab} - \mathbf{u}_{n,ab}. \quad (16)$$

The tangential unit vector is then

$$\mathbf{t}_{ab} = \frac{\mathbf{u}_{t,ab}}{|\mathbf{u}_{t,ab}|}, \quad (17)$$

and the tangential component of the collision force is defined as

$$\mathbf{f}_{col}^{t,a \rightarrow b} = -\mu_f |\mathbf{f}_{col}^{n,a \rightarrow b}| \mathbf{t}_{ab}. \quad (18)$$

The total collision force on a particle i is the sum of the collision forces from all particles j ,

$$\mathbf{F}_{col}^i = \sum_j \left(\mathbf{f}_{col}^{n,i \rightarrow j} + \mathbf{f}_{col}^{t,i \rightarrow j} \right). \quad (19)$$

Particle-wall collisions are determined by treating the wall as a particle, with a radius of zero and infinite mass.

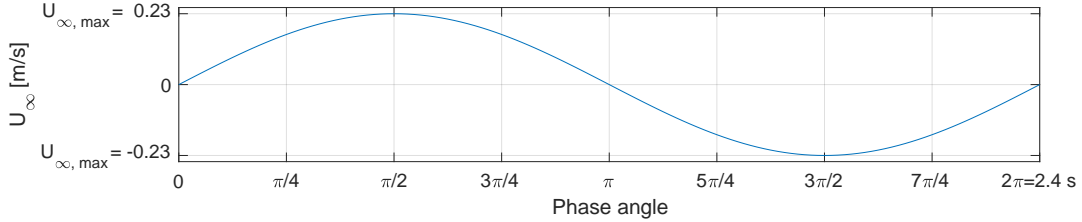


Figure 1: Time evolution of the freestream streamwise velocity. The period of oscillation is $T = 2.4$ seconds, and the maximum freestream velocity is $U_{\infty, \text{max}} = 0.23 \frac{\text{m}}{\text{s}}$.

4 Simulation Configuration & Methodology

The parameters of the numerical simulation are configured based on the work by Frank et al. [26] [25] [24]. The experiment was conducted in the small-oscillatory flow tunnel at the Sediment Dynamics Laboratory of the Naval Research Laboratory, Stennis Space Center, MS. The configuration of their experimental setup is shown in Frank et al. [26]. The square cross-sectioned, water-filled, closed channel is bound on the top and sides, and the bottom is made up of a sand bed. The average diameter of the sand is 0.7 mm, with an average density of 2635 kg/m^3 . Initially, the sand bed is roughly flat. The fluid is then forced to an oscillatory flow by a piston, with a prescribed period of 2.4 seconds. The maximum freestream velocity, shown in Figure 1 achieved by the flow is roughly 0.23 m/s. Eventually, a quasi steady-state condition is reached. At this point, ripples, of a roughly sinusoidal wavelength of 100 mm, and amplitude of roughly 20 mm, have formed in the bed, and their migration and wavelength evolution are on a timescale much larger than the period of oscillation. Data were collected for 11 complete oscillation periods. Using Particle Image Velocimetry (PIV), the three components of the velocity field are measured in a two-dimensional plane parallel to the streamwise and wall-normal directions, centered on a single ripple. In addition, the surface of the ripple is tracked using high speed cameras, and information about individual entrained grains is available.

In order to best approximate the experimental configuration, while maintaining computational feasibility, a Large-Eddy Simulation (LES) approach was chosen so that a courser grid could be utilized. The experimental tunnel is modeled as a channel flow between two parallel plates, which is periodic in both the streamwise and spanwise directions. The half-height of the channel, h , is used to describe the extants of the domain. As shown in Figure 2, the domain measures $4h$, $2h$, and h , in the streamwise, wall-normal, and spanwise directions, respectively. The grid is comprised of 256 by 128 by 64 nodes, in the streamwise, wall-normal, and spanwise directions, respectively. The streamwise and spanwise grids are uniform, and the wall-normal grid is stretched to be refined at the walls and in the rippled particle bed. In wall units, here denoted by a plus sign superscript, the grid is $x^+ = z^+ = 18$ and $y^+ = 10$, where x is the streamwise direction, z is the spanwise direction, and y is wall-normal. Although ideally y^+ should be on the order of a single wall unit, the literature [2] has shown that LES using this larger grid spacing is sufficient to capture the mesoscale features of the flow. This grid configuration allows for particle diameters of 1 mm. The wall at the bottom of the domain has a no-slip boundary condition and is covered in a sinusoidally rippled layer of particles. Gravity, 9.81 m/s^2 , acts in the negative y direction.

Per Hino et. al [31], the Stokes length Reynolds number, based on the Stokes thickness, is given by

$$Re_s = \frac{U_0 l_s}{\nu}, \quad (20)$$

where U_0 is the oscillating mean velocity component and the Stokes thickness is given by $l_s = \sqrt{\frac{2\nu}{\omega}}$. For smooth walls, Hino et. al found that the flow was stable and laminar for $Re_s < 400$,

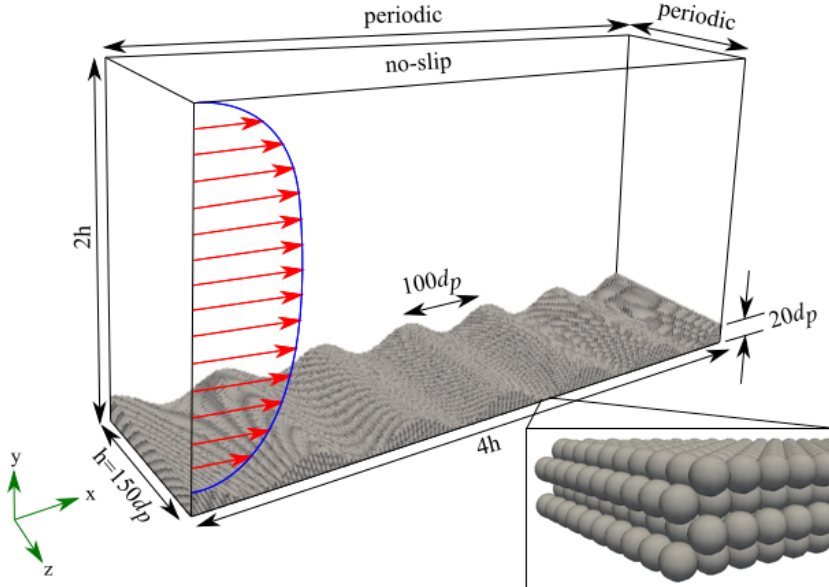


Figure 2: Initial configuration of the simulation. The flow is driven by a sinusoidal pressure gradient in the streamwise direction. The morphology of the particle bed is initially sinusoidal. The inset in the lower-right corner shows an example of the initial body-centered cubic packing configuration of the particle bed. The bed comprises six total ripples: five complete ripples are bookended by a split sixth ripple at the periodic streamwise boundary.

transitioning to turbulence for $400 < Re_s < 800$, and fully turbulent for $Re_s > 800$. In this work, $Re_s = 200$, which would put it squarely in the laminar regime. However, the interaction of the flow with the rippled morphology of the mobile particle bed generates coherent turbulent structures in the flow.

It should be noted that the numerical code used in this work has been shown to replicate ripple formation in unidirectional pipe flow, per Arolla and Desjardins [2]. However, due to the large timescale required, it would not have been computationally feasible to simulate the generation of ripples from a flat bed under an oscillatory flow. Therefore, since the experimental work results in a quasi-steady state, the particle bed is prescribed an initial sinusoidal ripple shape with a wavelength and amplitude best approximating the experimental configuration. The result is 1,540,800 total particles, which are packed in a body centered cubic (BCC) configuration, as shown in Figure 2. In order to maintain a similar Shields parameter, $\Theta = \frac{\tau_{bed}}{(\rho_p - \rho_f)gd_p}$, the particle diameter, d_p is 1 mm and the particle density, ρ_p , is 2500 kg/m³. The Shields parameter is a dimensionless number reflecting the relative effects of the erosive forces (shear stress) to the restorative forces (gravity). A high Shields parameter reflects highly erosive flow conditions, whereas a low value indicates a stable condition for the bed. Despite the tightly packed spacing of the particle bed, the spring-dashpot particle model will force the bed to compress under the effect of gravity. In order to make sure that this process is isolated from any erosive behavior caused by the oscillatory flow, the bed is allowed to settle under the effect of gravity alone. Therefore, the full simulation domain is initialized with a zero velocity field, and no pressure gradient forcing. The particles then settle into an equilibrium state with the effect of gravity and the bottom wall. Since the bed is initialized in a close-packed structure, the settling process only compressed the particles, but does not cause reshuffling. The final, settled, particle bed is stable and roughly sinusoidal. Once the bed has been stabilized under gravity, the oscillating pressure gradient is implemented, driving the flow and distorting the bed. The shear stress at the rippled bed interface is monitored until it converges, which takes 3 full periods, at which point it is assumed that a quasi-steady state has been achieved.

5 Results

5.1 Data Analysis

Although the experimental data are two-dimensional, and are limited to a single ripple, the numerical work is fully three-dimensional and spans six ripples. Therefore, in order to better compare the datasets, the numerical data are averaged three ways to produce two-dimensional data over a single canonical ripple. Per the work of Scotti and Piomelli [43], the first type of averaging is done spatially over planes of homogeneity (x - z planes), to generate two-dimensional data. The second is an ensemble approach, which spatially averages all six ripples down to a single ripple. The third is a temporal phase averaging. The following operator combines the spatial plane averaging and the ensemble spatial averaging, reducing the data to two-dimensions and a single ripple,

$$\underline{f}(x, y, t) = \sum_{r=1}^6 \frac{1}{TrL_{\lambda_r}L_z} \int_0^T \int_0^{L_{\lambda_r}} \int_0^{L_z} f(x, y, z, t) dx dz dt. \quad (21)$$

T is the time over which the function is integrated, λ_r is wavelength of each of the ripples, and L_z is the spanwise width of the domain. The temporal phase averaging, which highlights the influence of the variable pressure gradient, is identified as

$$\langle f \rangle(x, y, t) = \frac{1}{TL_{\lambda_r}L_z} \sum_{n=1}^N \int_0^{L_{\lambda_r}} \int_0^{L_z} f(x, y, z, t + nT) dx dz. \quad (22)$$

As noted, the experimental data was collected for eleven periods, therefore the analysis of the experimental data is also phase averaged. Thus, both the numerical and experimental datasets are two-dimensional and span only a single ripple. Since all analysis will use these forms of the data, going forward, the underline and angle brackets will be omitted for simplicity.

5.2 Flow Evolution: Vorticity & Velocity Streamlines

Per Bagnold [3], the ripples in this work are classified as “vortex ripples”, as they have achieved sufficient amplitude to shed vortices under oscillatory flow. Although it is commonly used as a method of vortex identification, the Q-criterion of Chong and Perry [14], is not used in analyzing the experimental data (but will be used to identify three-dimensional vortical structures in the numerical data). Instead, the vorticity, defined as the curl of the velocity field, $\omega = \nabla \times \mathbf{u}_f$, and describing the local spinning motion of the fluid, does a better job in this case of identifying the mechanisms of the flow. Comparing the vorticities of the numerical and experimental data immediately highlights the similarities of the two flows. It should be noted that vorticity does not discern between shear and vortical components, however.

Per Figure 3, at the beginning of the period, phase time 0, a detached vortex can be seen to the left of the ripple, as it was shed from the ripple as the accelerated from right to left. Although the freestream velocity at this phase is roughly zero, there are clearly non-zero velocities at the bed interface. As the flow accelerates from left to right, this vortex is seen to decay and get swept away by the shear layer that has formed on the upstream face and crest of the ripple at phase time $\frac{\pi}{4}$. At phase time $\frac{\pi}{2}$, the freestream velocity has reached its maximum and the shear layer has continued to grow while the original vortex has been broken up by the freestream. At phase time $\frac{3\pi}{4}$, the flow is still moving from left to right, but is decelerating. The shear layer has developed into a vortex as it is shed on the downstream side of the ripple crest. When the freestream velocity has decelerated back to zero at phase time π , the vortex has detached completely from the ripple crest. Expectedly, the second half of the oscillation period mirrors the same processes at the first half, but in the opposite direction.

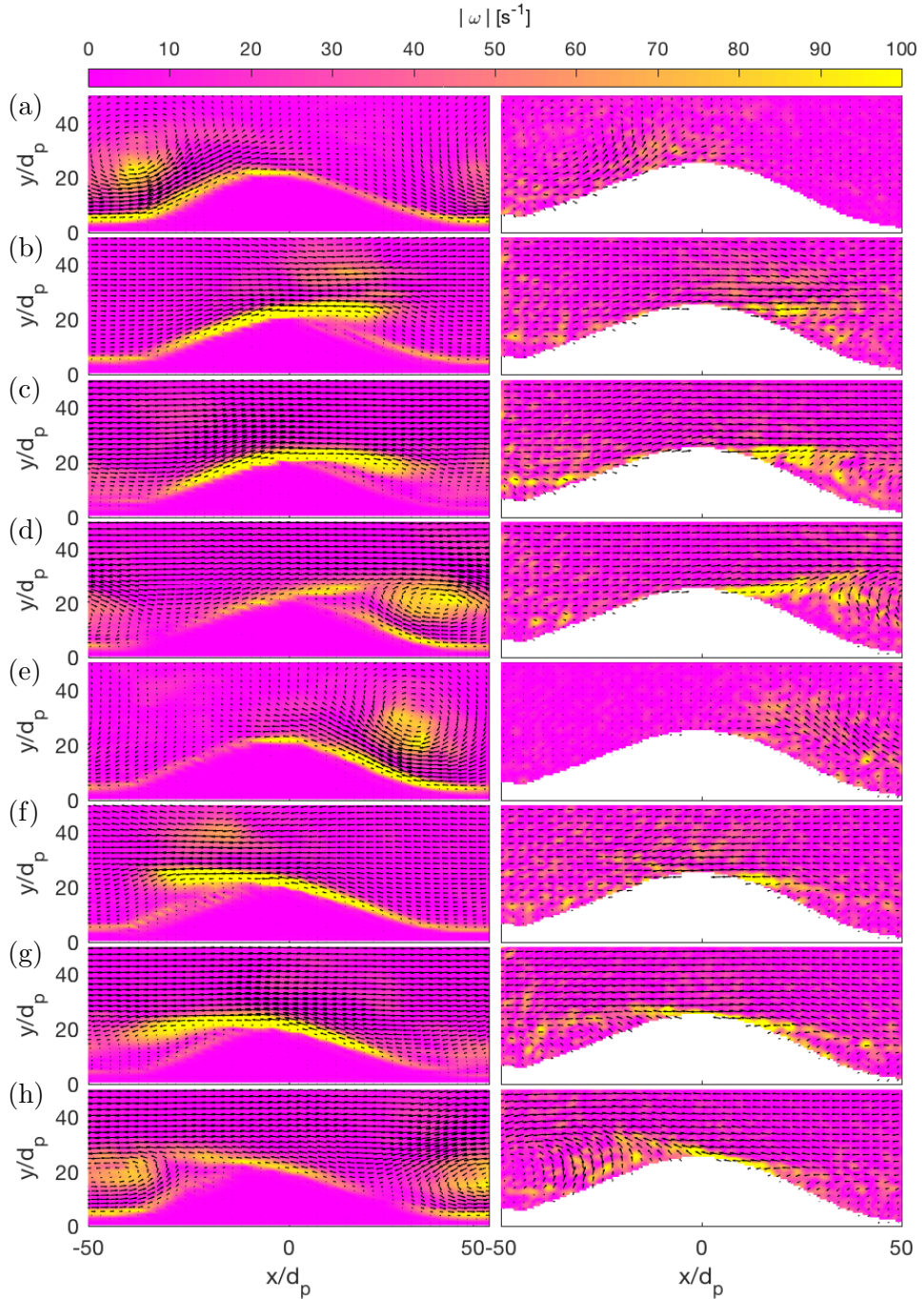


Figure 3: Comparison of the numerical (left column) and experimental (right column) vorticities. The absolute value of the vorticity is used to better illustrate the similarities in shear and vortical structures between the two datasets. Phase times: (a) $\frac{0\pi}{4}$ (a) $\frac{1\pi}{4}$ (a) $\frac{2\pi}{4}$ (a) $\frac{3\pi}{4}$ (a) $\frac{4\pi}{4}$ (a) $\frac{5\pi}{4}$ (a) $\frac{6\pi}{4}$ (a) $\frac{7\pi}{4}$.

The vorticities of the numerical work reflect the behavior of the vortices in the experimental data. Although the numerical vorticity is much smoother, due to additional averaging, the experimental data does show good quantitative agreement. In Figure 3, both datasets show that the shear layer formed on the stoss side of the ripple can be seen most clearly at phase time $\frac{\pi}{2}$ and $\frac{3\pi}{2}$ (in the opposite direction). At phase time $\frac{3\pi}{4}$, a section of vorticity is shedding off the lee side of the ripple. Although the source of this high concentration is unclear from the vorticity plot alone, the overlayed velocity vector field shows that this high level of vorticity is

indeed a vortex. This is also made clear at phase time $\frac{7\pi}{4}$, in the opposite direction.

Constant velocity streamlines help to further confirm the processes of the flow. Figure 4 shows the velocity vector fields and velocity streamlines for both the numerical and experimental flows, respectively. In both cases, a vortex is clearly identified at phase time 0. The numerical vortex, having been shed when the flow was oriented right to left, is centered roughly $40d_p$ to the left of the ripple crest and $30d_p$ in the wall-normal direction. The experimental vortex is centered roughly $35d_p$ to the left of the ripple crest and $35d_p$ in the wall-normal direction. At phase times $\frac{\pi}{4}$, $\frac{\pi}{2}$, and $\frac{3\pi}{4}$, the separated flow indicates a shear layer becoming a vortex. At phase time $\frac{7\pi}{4}$, this vortex, albeit in the opposite direction, is clearly identifiable as forming in the wake of the separated flow. The numerical data shows this particularly well at phase time $\frac{3\pi}{2}$. Overall, the numerical results show very good qualitative agreement with the experimental work. The LES is able to capture the formation of the shear layer on the upstream side of the ripple, which develops into a vortex on the downstream side, and is shed into the valley between ripples.

Here, the extent of the numerical domain provides some additional insight. Rather than examine the heavily averaged flow field about a single isolated ripple, Figure 5 shows the evolution of instantaneous vorticity in a single x-y plane spanning three ripple wavelengths. The shear layer formed at the fluid-bed interface between phase times 0 and $\frac{2\pi}{12}$ (the top three panels of Figure 5) detaches from the interface starting around phase time $\frac{\pi}{4}$. As the fluid is turbulent, the exact timing and the magnitude of the detachment can vary greatly. At phase time $\frac{4\pi}{12}$ (the fifth panel from the top in Figure 5), the shear layers on the ripples centered at $x = 0d_p$ and $x = 200d_p$ are strongly detached from the ripple peaks. Whereas the shear layer on the ripple centered at $x = 100d_p$ has hewn much closer to the downstream ripple face. By phase time $\frac{7\pi}{12}$ (the bottom panel in Figure 5), the shear layer shed from the ripple at $x = 0d_p$ has broken up sufficiently to not form a clear shear layer on the adjacent ripple at $x = 100d_p$. In contrast, the shear layer shed from the ripple at $x = 100d_p$ has remained intact and formed a strong shear layer on the upstream face of the adjacent ripple at $x = 200d_p$. This phenomenon has important consequences on the particle motion at the interface, as discussed in Section 5.7.

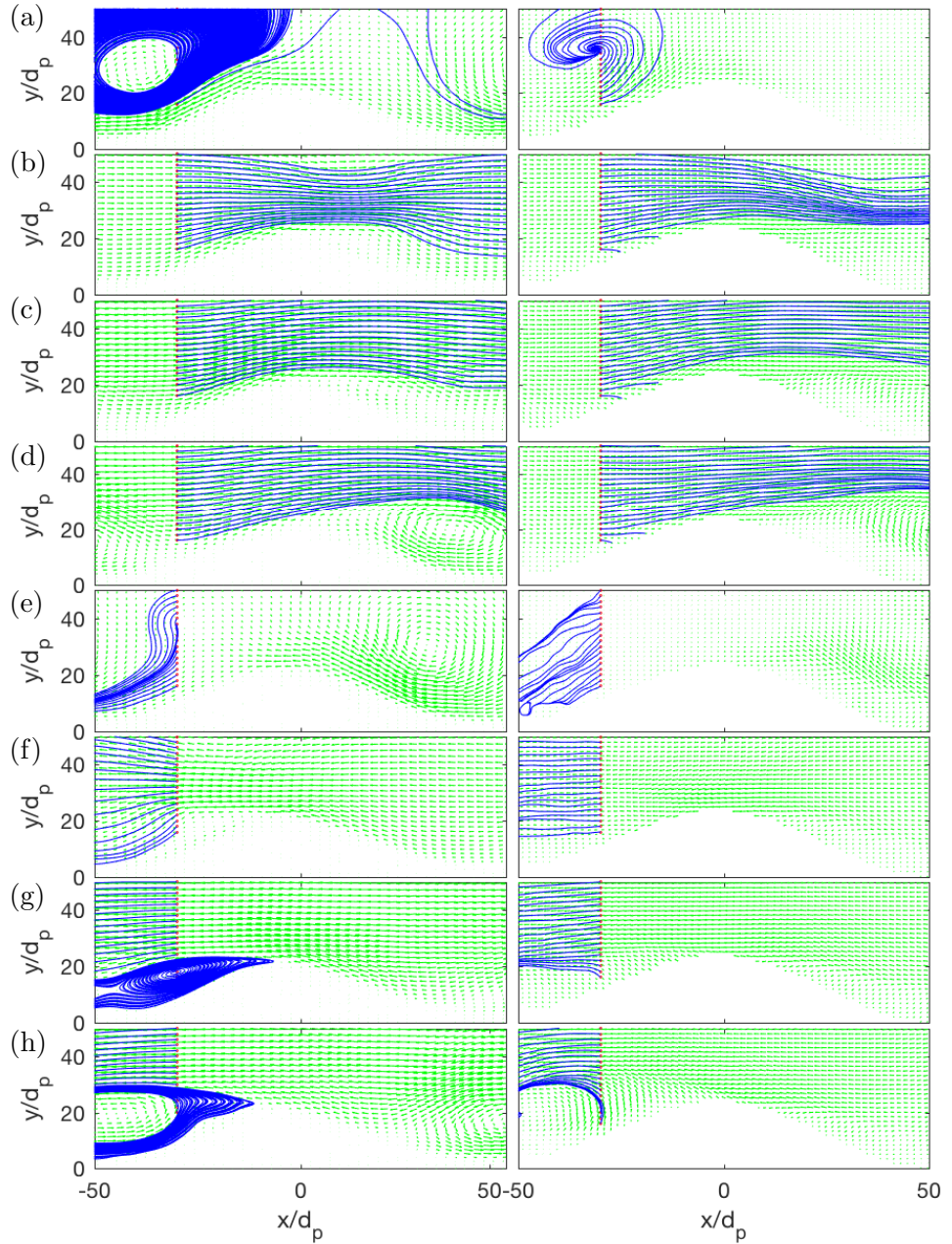


Figure 4: Comparison of the numerical (left column) and experimental (right column) velocity streamlines overlayed on corresponding velocity fields. Phase times: (a) $\frac{0\pi}{4}$ (a) $\frac{1\pi}{4}$ (a) $\frac{2\pi}{4}$ (a) $\frac{3\pi}{4}$ (a) $\frac{4\pi}{4}$ (a) $\frac{5\pi}{4}$ (a) $\frac{6\pi}{4}$ (a) $\frac{7\pi}{4}$.

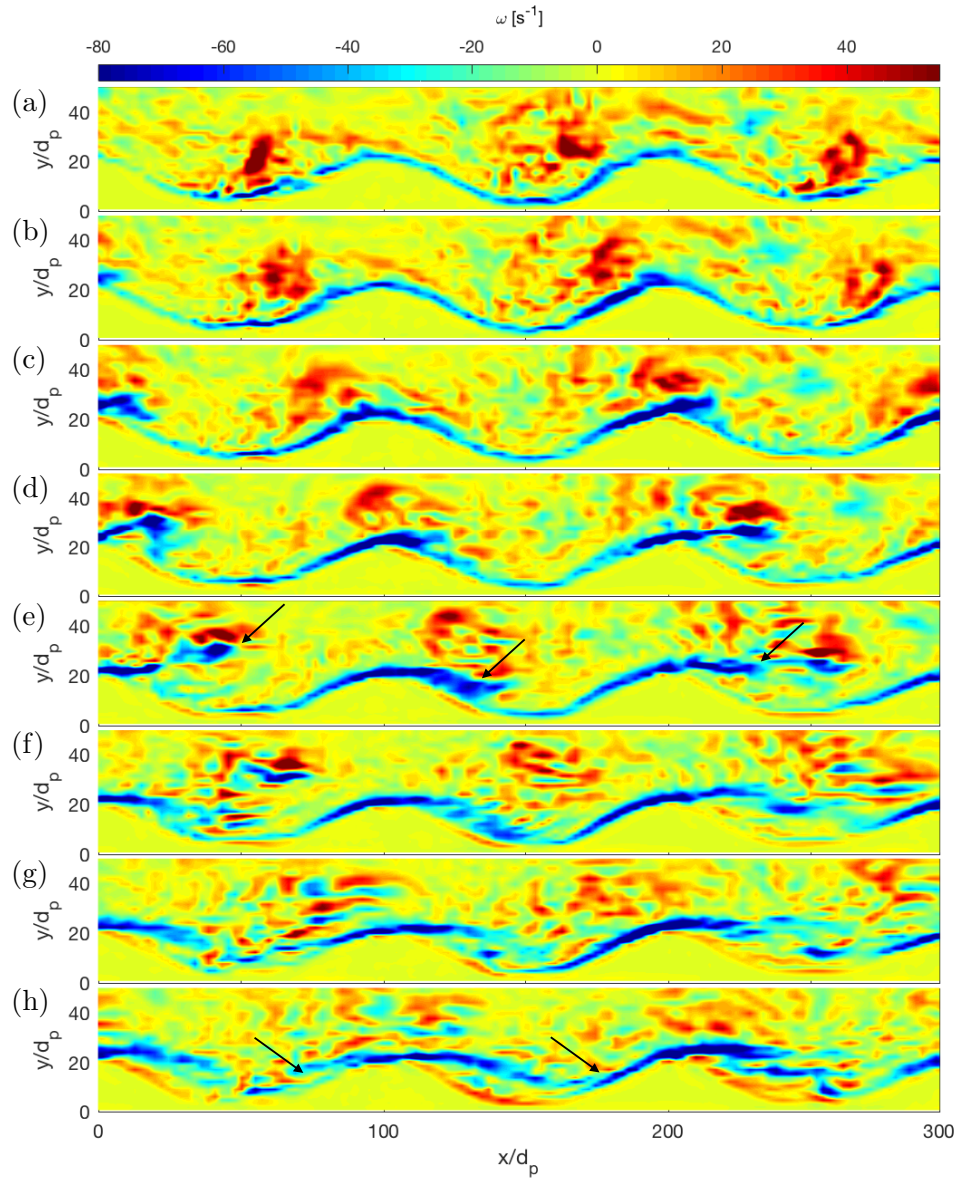


Figure 5: Numerical vorticity in an x-y plane at $z = 42d_p$. Shown from the beginning of the oscillation period (phase time 0) to just after the flow reaches the maximum free stream velocity (phase time $\frac{7\pi}{12}$). Phase times: (a) $\frac{0\pi}{12}$ (a) $\frac{1\pi}{12}$ (a) $\frac{2\pi}{12}$ (a) $\frac{3\pi}{12}$ (a) $\frac{4\pi}{12}$ (a) $\frac{5\pi}{12}$ (a) $\frac{6\pi}{12}$ (a) $\frac{7\pi}{12}$. The arrows at phase times $\frac{4\pi}{12}$ and $\frac{7\pi}{12}$ indicate points of interest related to the shear layer detachment and reattachment, respectively.

5.3 Flow Evolution: Vortex Identification

Although vorticity quantifies the swirling effects of the flow, it cannot discern between shear and vortices. Per the work of Chong et al. [14], the flow of a continuum can be completely categorized by the invariants of the rate of deformation tensor. In identifying vortical structures in a flow, this tensor is the velocity gradient tensor, $\nabla \mathbf{u}_f$. The second invariant of the velocity gradient tensor, Q , contains squared measures of both the rate of strain and rotation tensors, $Q = \frac{1}{2}(P^2 - S_{ij}S_{ji} - \Omega_{ij}\Omega_{ji})$. Therefore, when $Q > 0$, the flow is dominated by rotation at that location, and when $Q < 0$, the flow is dominated by shear. Figures 6 and 7 show iso-contours of the second invariant Q over the first half of an oscillation period. At phase time 0, distorted and detached spanwise vortices are seen on the lefthand side of the ripple faces, as they have just been shed from flow moving from right to left. At phase time $\frac{\pi}{4}$, the flow accelerates from left to right, and these spanwise vortices are broken up and ejected away from the bed. By phase time $\frac{\pi}{2}$, the freestream velocity has reached its maximum and the near bed unsteady flow is dominated by streamwise structures in the shear layer, mostly forming on the stoss side of the ripples. As the flow decelerates at phase time $\frac{3\pi}{4}$, the streamwise structures are converted into spanwise vortical structures which begin to form on the lee side of the ripples. By the time the freestream velocity is back to zero at phase time π , these distorted spanwise vortices have detached from the ripples and can be seen on the righthand side of the crest ripples, mirroring the detached vortices at phase time 0.

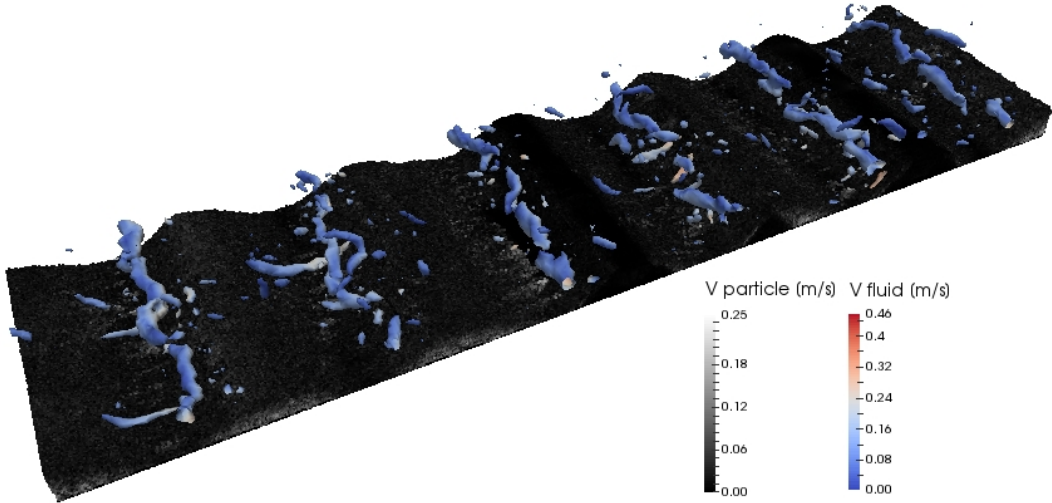


Figure 6: Numerical Q-criterion isocontours, colored by the fluid velocity, at phase time 0. Freestream velocity is zero.

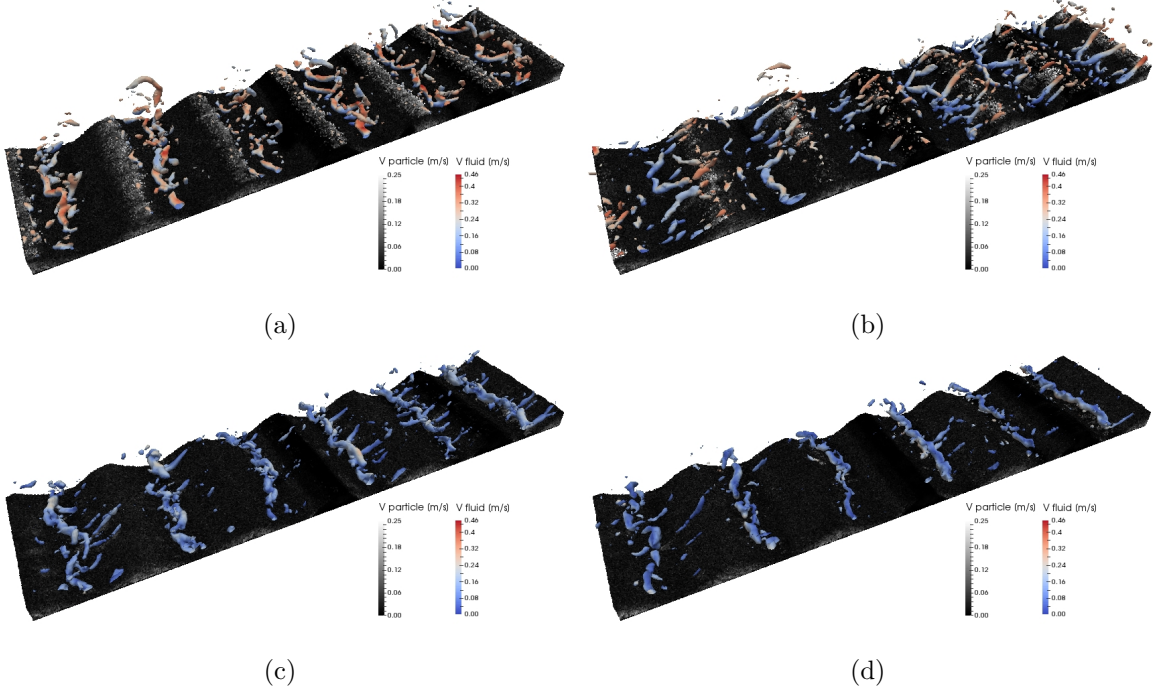


Figure 7: Numerical Q-criterion isocontours, colored by the fluid velocity. (a) Phase time $\frac{\pi}{4}$. The fluid is accelerating from left to right. (b) Phase time $\frac{\pi}{2}$. The fluid has achieve maximum freestream velocity, from left to right. (c) Phase time $\frac{3\pi}{4}$. The fluid is decelerating, but is still moving from left to right. (d) Phase time π . The freestream velocity has decelerated to zero, and is about to begin accelerating from right to left.

5.4 Wall-Normal Flow Statistics

Two approaches are used to compare the wall-normal flow statistics of the experimental and numerical data. The first consists of wall-normal statistics located at the ripple crest, ripple trough, and half way up the left-hand side ripple face. The second compares wall-normal statistics that are spatially averaged over the entirety of the ripple wavelength, which results in a single wall-normal profile for any given statistic. This approach analyzes the effective roughness of the wall on a macroscopic scale. It should be noted that because the numerical simulation solves the volume-filtered Navier-Stokes equations everywhere in the domain, \mathbf{u}_f data is available everywhere, including “within” the ripple. Therefore all the numerical wall-normal statistical profiles span all the way down to the bottom wall. The experimental data does not include fluid velocity data within the ripple, therefore, it is not shown. So where applicable, the experimental wall-normal statistical profiles are shown only where data was recorded. In these cases, the profiles may not extend all the way to the bottom wall.

The top three panels of Figure 8 compare the wall-normal streamwise velocity profiles at the ripple crest, face, and trough, respectively. The streamwise velocities are normalized by the maximum freestream velocity, U_∞ , and the wall-normal location is normalized by h . On the whole, the numerical model does a good job of predicting the velocity profile at the crest and face. However, at the ripple trough, the numerical model seems to overpredict the magnitude of the inflection point velocity. Of course, the ripple shape in the experiment is not completely sinusoidal, as in the numerical work, and the troughs are where the morphologies differ the most. Therefore, it is not surprising to see discrepancies in the profiles, particularly at the ripple trough. Spatially averaging the streamwise velocity profiles over the entire wavelength of the ripple treats the ripple effectively as surface roughness. The bottom panel of Figure 8 shows that trends of the experimental work are captured by the numerical model, albeit with a

consistent slight over-prediction of the magnitude of the streamwise velocity.

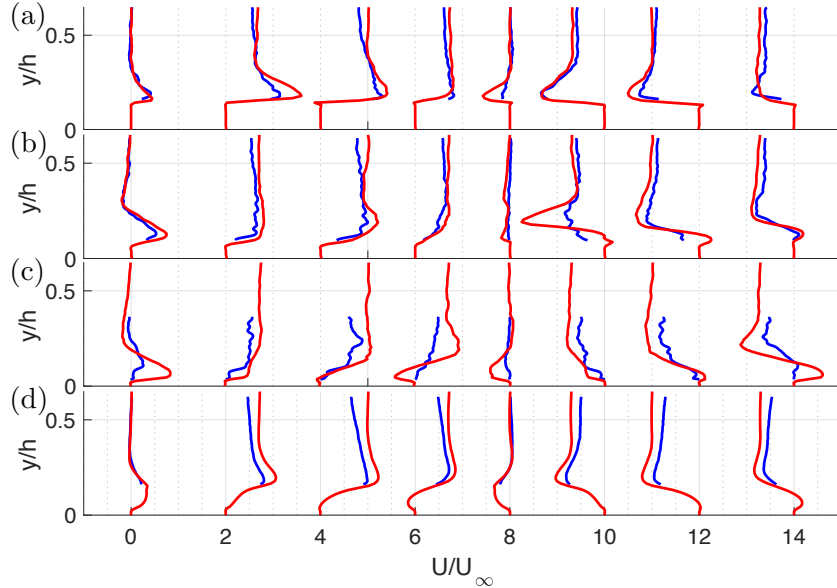


Figure 8: Streamwise velocity profiles in the wall-normal direction, shown from left to right at phase times $\frac{n\pi}{4}$, for $n = 0, 1, \dots, 6, 7$, where each phase angle is shifted on the x-axis. Profiles shown at: (a) the ripple crest; (b) halfway up the ripple face; (c) the ripple trough; (d) averaged over the wavelength of the ripple to approximate the macroscale “roughness” of the fluid-bed interface. The velocity is normalized by the maximum achieved freestream streamwise velocity, U_∞ . The wall-normal position is normalized by the half-height of the channel, h . The experimental results are denoted by a blue line, and the numerical results by a red line. In some cases, the range of the PIV data was limited, therefore, the entire profile was not available.

In order to examine the deviations from these averaged velocities, the turbulent kinetic energy (TKE) and the Reynolds shear stress, $\langle u'_i u'_k \rangle$. As was done with the velocity profiles, spatially averaging the profiles of the quantities over the entire wavelength of the ripple treats the ripple effectively as surface roughness. The top panel of Figure 9 shows that trends of the experimental work are captured by the numerical model, albeit with a consistent slight over-prediction of the magnitude of the streamwise velocity. Not only are the magnitudes of the TKE profiles consistent, but the shape of the curves show good agreement between the experimental and numerical work. Again, like the velocity profiles, the numerical model very slightly over predicts TKE in most phases and locations. The bottom panel of Figure 9 shows that qualitative trends in the profiles of the Reynolds shear stress are also well predicted by the numerical model, with some deviation in the location and magnitude of maximum values.

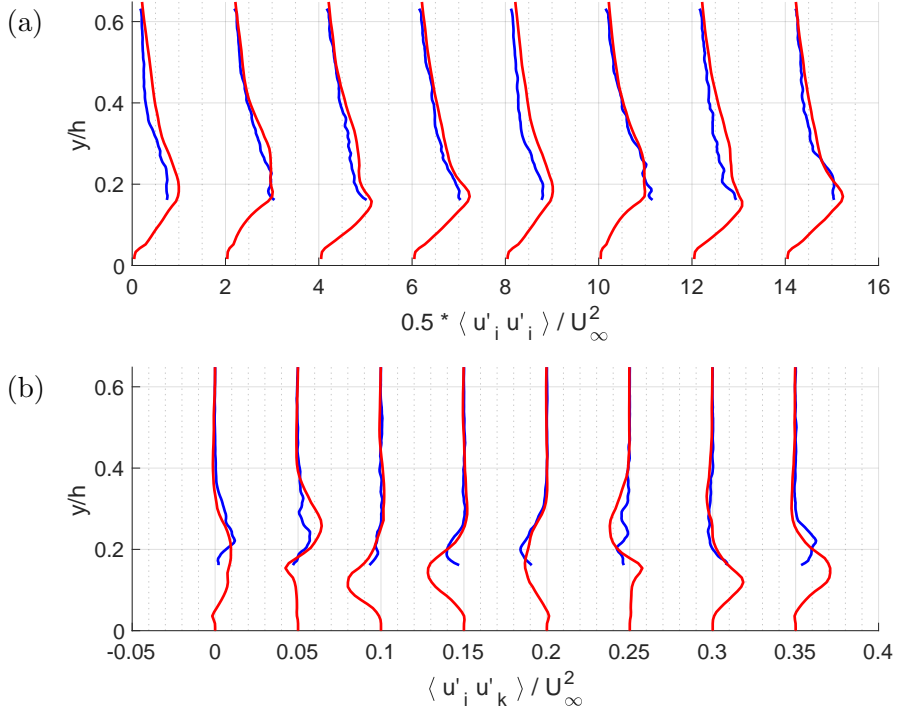


Figure 9: Wall-normal profiles of (a) the TKE, and (b) Reynolds Stress, averaged over the entire wavelength of the ripple to approximate the macroscale “roughness” of the fluid-bed interface. From left to right, the profiles are shown at phase angles $\frac{n\pi}{4}$, for $n = 0, 1, \dots, 6, 7$, where each phase angle is shifted on the x-axis. In both cases, the values are normalized by the square of the maximum achieved freestream streamwise velocity, U_∞ . The wall-normal position is normalized by the half-height of the channel, h . The experimental results are denoted by a blue line, and the numerical results by a red line. In some cases, the range of the PIV data was limited, therefore, the entire profile was not available.

5.5 Fluid-Bed Interface

Determining the location of the fluid-bed interface is crucial, not only in tracking the evolution of the bed morphology, but also in accurately calculating the bed shear stress. A couple different methods were tested, including dividing the domain into square bins of size d_p , then comparing all particles in each bin to determine where the bed ended, and where the fluid started. This meant defining a threshold, above which it was assumed all particles were not a part of the bed, but rather were entrained. However, this method proved unable to consistently provide an accurate interface location, as the definition of the threshold was problematic. Relying solely on particle velocity and/or angular velocity also proved unreliable, as a particle could momentarily be stationary, but still be entrained, or above the threshold, but still moving slowly. The best results were found using the approach of Kidanemariam and Uhlmann [33]. They defined a spanwise averaged two-dimensional solid volume fraction function, equivalent to $\langle(1 - \psi_f)\rangle$, defined now as $\langle\psi_p\rangle$. The authors defined the threshold at $\langle\psi_p\rangle_{threshold} = 0.1$, such that the two-dimensional interface is

$$h_b(x, t) = y, \quad \text{where } \langle\psi_p\rangle = \langle\psi_p\rangle_{threshold}. \quad (23)$$

Figure 10 shows the $\langle(1 - \psi_f)\rangle$ field and the fluid-bed interface at phase time $\frac{\pi}{4}$. Other methods that were abandoned would routinely report interfaces closer to $\langle\psi_p\rangle_{threshold} = 0.3$. As such, non-moving particles were considered to be above the fluid-bed interface, leading to spurious erosion statistics.

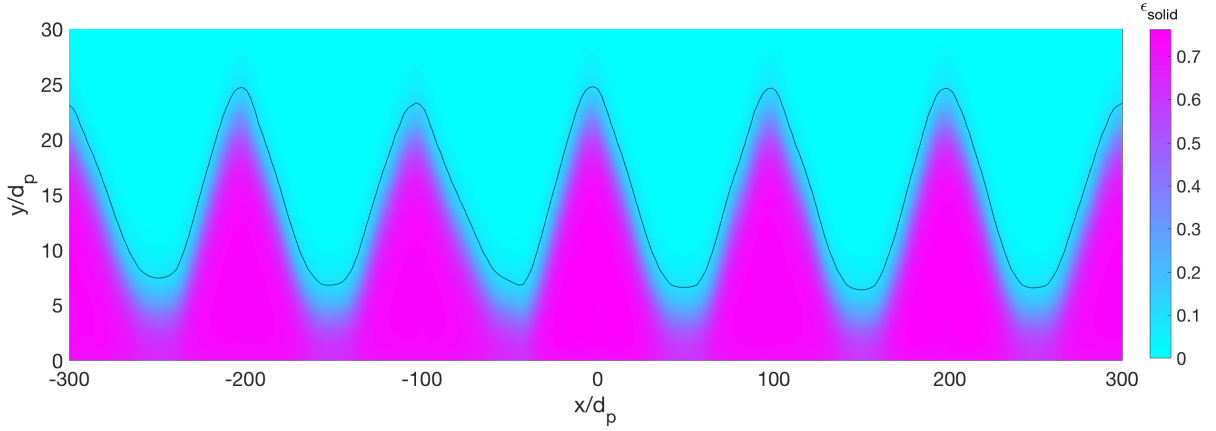


Figure 10: Numerical mean fluid-bed interface, as determined by assuming the bed has a solid volume fraction $\langle \psi_p \rangle \geq \langle \psi_p \rangle_{threshold}$. The data is shown at phase time $\frac{\pi}{4}$, and has been normalized by the particle diameter.

5.6 Ripple Shape

As discussed in Section 5.1, the numerical data has been spatially, ensemble, and phase-averaged to produce a two-dimensional data for a single canonical ripple. This applies to the fluid and solid phases of the LES. In the experimental work, the two-dimensional fluid data is phase-averaged over 11 periods. The fact that the initial numerical ripple shape is modeled as symmetric, when the experimental ripple is not, provide opportunity for discrepancy between the two data sets. Despite these potential issues, the numerical model does a good job qualitatively predicting the behavior of the ripple shape. It should be noted that overall shape and wavelength of the ripples do not change on a macroscopic scale, thus they are quasi steady-state. The bulk of the ripple evolution is confined to the peaks. In Figure 11, the ripple shapes are shown over an entire flow oscillation period. At phase time 0, the ripples are skewed to the left of “center” of the ripple, defined at $x = 0$, with a sharper face angle on the left side than on the right. Once the flow is accelerated from left to right, the peak becomes more symmetric and more centered, as the particles at the peak are affected by the shear layer generated on the stoss side of the ripple. By phase times $\frac{\pi}{2}$ and $\frac{3\pi}{4}$, the peak has shifted to the right of center and now the sharper face angle is to the right of center, mirroring the morphology of phase time 0. At phase time π , the flow has decelerated back to a freestream velocity of zero, and the ripple shapes are retained. As the flow reverses, the same processes of the first half of the oscillation period are mirrored, until the initial ripple shape is recovered at phase time $\frac{7\pi}{4}$. Qualitatively, the numerical model is able to capture this phenomena. Quantitatively, the DPM does a good job of predicting the overall shape and height of the experimentally measured ripple. It should also be noted that the numerical data shows that the swaying of the ripple peak is not exactly centered about the origin. This asymmetry is attributed to the fact while the simulation converged, the net effect of the flow on the ripple was not symmetrical as the flow transitioned from laminar to more turbulent over time.

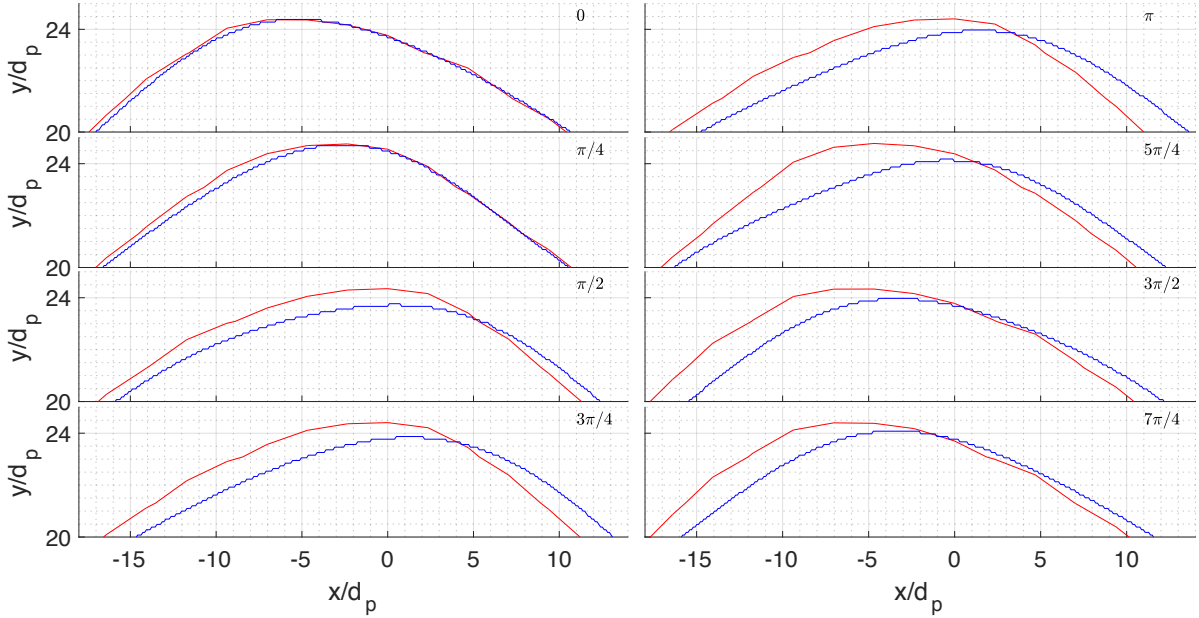


Figure 11: Experimental and numerical ripple comparison. The data has been normalized by the particle diameter. The blue line denotes experimental data, the red line denotes numerical data. The phase angle is denoted in the upper-right corner of each panel.

5.7 Suspended Load

As described in Section 5.3, a shear layer forms on the upstream side of each ripple as the fluid accelerates. Then, as the flow decelerates to zero before changing direction, the shear layer develops into a spanwise vortex which is shed to the downstream side of the ripple. During the acceleration phase of the period, the shear layer imparts momentum to the particles at the face of the upstream side of the ripple. This results in a spectrum of particle behavior, ranging from slight particle oscillation, but no net displacement, up to short timescale particle suspension (entrainment/saltation) resulting in particle relocation from the upstream face to the downstream face of a ripple. In this section, the suspended load is examined separately from the bed load (rolling and/or sliding, reptation) in order to more closely complement the experimental sediment data. Good qualitative agreement is observed with the experimental sediment results (shown explicitly in Frank et al. [26]).

Figure 12 shows an isolated ripple at phase time $\frac{\pi}{4}$. The spanwise vortex has already been mostly shed from the ripple peak, and some particles are seen to be entrained by the flow. The fluid-bed interface, as defined by the solid volume fraction in Section 5.5, is shown as a solid grey surface in order to better visualize the particles which are determined to be suspended in the flow. Those particles entirely above the surface are considered to be fully entrained by the fluid.

Also, it should be noted that although a particle may be identified as suspended at phase time $\frac{\pi}{4}$ does not mean that it will be identified as suspended at any other point in the oscillation period. In fact, in a single period, those particles identified as suspended at either time of maximum flow acceleration ($\frac{\pi}{4}$ and $\frac{5\pi}{4}$), are, in fact, only identified at one time or the other, but almost never both. However, those particles do generally continue to move throughout the period, but usually in the bed load regime (which is discussed in Section 5.8), rather than the suspended load regime.

To understand the behavior of the suspended load, the particle pathways are shown for the first half of an oscillation period in Figure 13. Shown are the ripple profile, the bottom-up view of vortical structures at phase time $\frac{\pi}{4}$, and the half oscillation period pathways of the

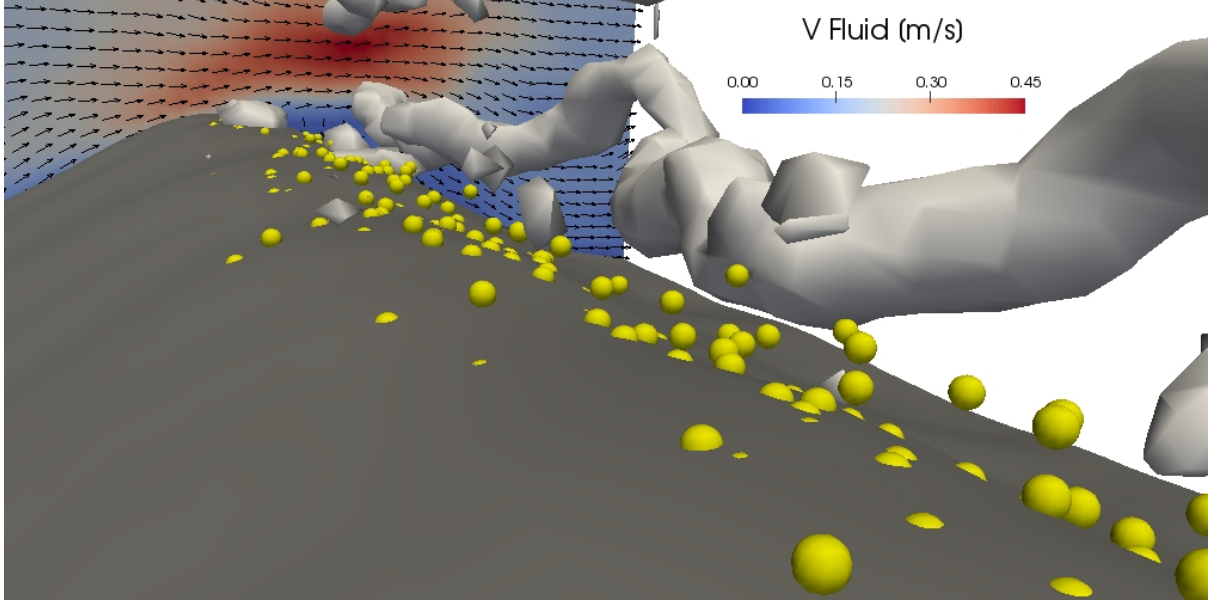


Figure 12: An isolated ripple is shown at phase time $\frac{\pi}{4}$. The fluid-bed interface is shown as a solid surface in dark grey. The spanwise vortex, shown as an iso-contour of the Q-criterion, is just being shed to the downstream side of the ripple. The particles are colored in yellow to highlight those particles which have been pulled from the fluid-bed interface and suspended in the flow.

particles which have been entrained at phase time $\frac{\pi}{4}$ (blue lines) and $\frac{7\pi}{12}$ (red lines). The dotted line at $z = 42d_p$ indicates the x-y plane at which instantaneous vorticities are shown in Figure 5. As discussed in Section 5.2, when the shear layers detach from the ripple peaks, they can either break up or stay close to the interface and combine with the shear layer on the adjacent downstream ripple. Therefore, two distinct maximums in the momentum transfer from the fluid to the particles on the ripple faces are observed. The peak momentum transfer occurs at phase time $\frac{\pi}{4}$ when the shear layer is first shed from the ripple peak. The second weaker wave of momentum transfer occurs due to the impact of shear layer shed from the upstream adjacent ripple, around phase time $\frac{7\pi}{12}$.

The actual pathways for particles entrained at phase time $\frac{\pi}{4}$ from Figure 13 (blue lines) are quantified in Figures 14 and 15. The pathways have been normalized in the spanwise direction. Therefore, the initial spanwise position for all entrained particles is $z = 0$. So the streamwise and wall-normal locations are retained relative to the ripple peak, and the spanwise locations have been equated. Both the numerical data, and the experimental work shown in Frank et al. [26], display similar particle pathways. Suspended particles are drawn into the fluid before landing about halfway down the downstream face of the ripple. The mean entrained particle starts about $10d_p$ to the left and $3d_p$ down from the particle peak. One standard deviation from the mean start location reflects about a $2.5d_p$ range in the wall-normal direction and a $5d_p$ range in the streamwise direction. The final position is roughly $12d_p$ to the right, and $7d_p$ down, from the ripple peak. At the final location, one standard deviation reflects a greater range than at the initial position, about $4d_p$ variation in the wall-normal direction and $8d_p$ in the streamwise direction.

Figure 16 further breaks down the the positions of all suspended particles over the course of a half oscillation period. The four figures on the left describe the motion of the particles determined to be suspended at the phase time indicated on the x-axis. So, each phase time characterizes the particles determined to be suspended *only* at that phase time. Therefore, the particles described at phase time $\frac{\pi}{4}$ may be different than those in an adjacent phase time

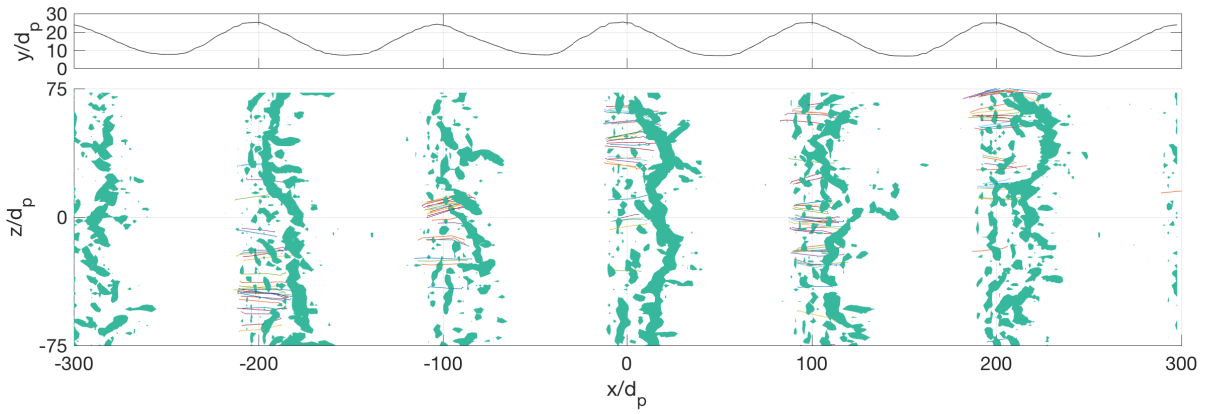


Figure 13: Phase time = $\frac{\pi}{4}$. The top panel shows the mean ripple shape. The bottom panel shows a view from the bottom-up (positive y direction perspective) of coherent structures, which will become spanwise vortices, being shed from the ripple peaks. The fluid structures are shown as the Q-criterion, which are solid colored. The solid lines denote the motion of entrained particles over the first half of an oscillation period.

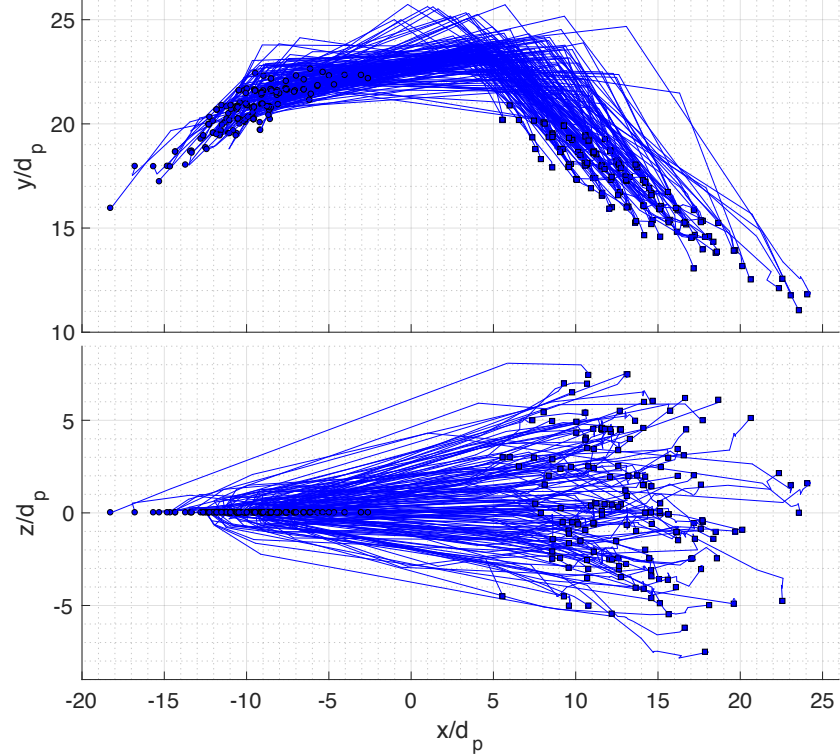


Figure 14: Two views of the suspended particle pathways over a single half oscillation period for particles determined to be entrained at phase time $\frac{\pi}{4}$. Top panel shows x-y perspective, and the bottom panel shows the x-z perspective. Pathways have been normalized for an initial spanwise direction ($z = 0$). Initial and final particle positions at phase times 0 and π , respectively, are denoted by circles and squares.

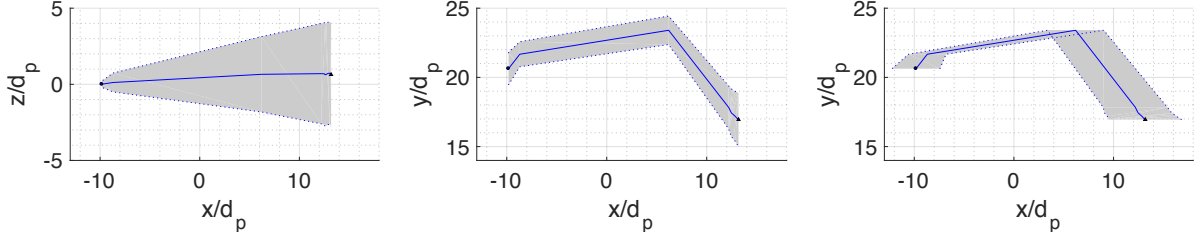


Figure 15: Suspended particle mean particle pathways and corresponding shaded standard deviation range. Initial and final particle positions at phase times 0 and π , respectively, are denoted by circles and squares.

column, since a particle may be suspended at one phase time, but may be static or in the bed load regime at any other phase time. In contrast, the four figures on the right *only* show the evolution of the motion of particles suspended at phase-time $\frac{\pi}{4}$. Particles determined to be suspended at $\frac{\pi}{4}$ are thus tracked over the half oscillation period (i.e. these mostly only move around phase time $\frac{\pi}{4}$, with particle velocity hovering around zero the rest of the phase times), and particles suspended at any other phase time are not shown.

Figure 16 makes clear that the maximum streamwise particle displacement occurs at phase time $\frac{\pi}{4}$ as expected, since this is the time of maximum fluid acceleration. Particles are drawn up over the ripple peak and deposited on the other side, which can be identified in the second row, where wall-normal Δy grows positive before becoming negative. And the spread of spanwise displacement is essentially symmetrical about the normalized initial positions. The bottom row shows that maximum particle velocities are roughly equal to the maximum freestream velocity. This is observed at the time of maximum fluid acceleration, again at phase time $\frac{\pi}{4}$, and shows good agreement with the sediment velocities observed in the experimental work, which are shown explicitly in Frank et al. [26]. Finally, there is a distinct, smaller peak in particle motion and velocity observed at phase time $\frac{7\pi}{12}$, which is due to the impact of the detached shear layer shed from the adjacent upstream ripple, as described in Section 5.2.

Since the particles are tracked in a Lagrangian framework, all of the forces acting on each particle are available. Therefore, the Shields parameter for each particle was calculated as the ratio of disturbing forces, f_{dist} , to restorative forces, f_{rest} ,

$$\Theta = \frac{\sum f_{dist}}{\sum f_{rest}}. \quad (24)$$

For particle diameters of 1 mm, the critical Shields value is roughly $\Theta_c = 0.05$. Saltating particles are observed to have $\Theta > 0.08$. And, non-moving particles are observed to have Shields parameter values below the critical threshold.

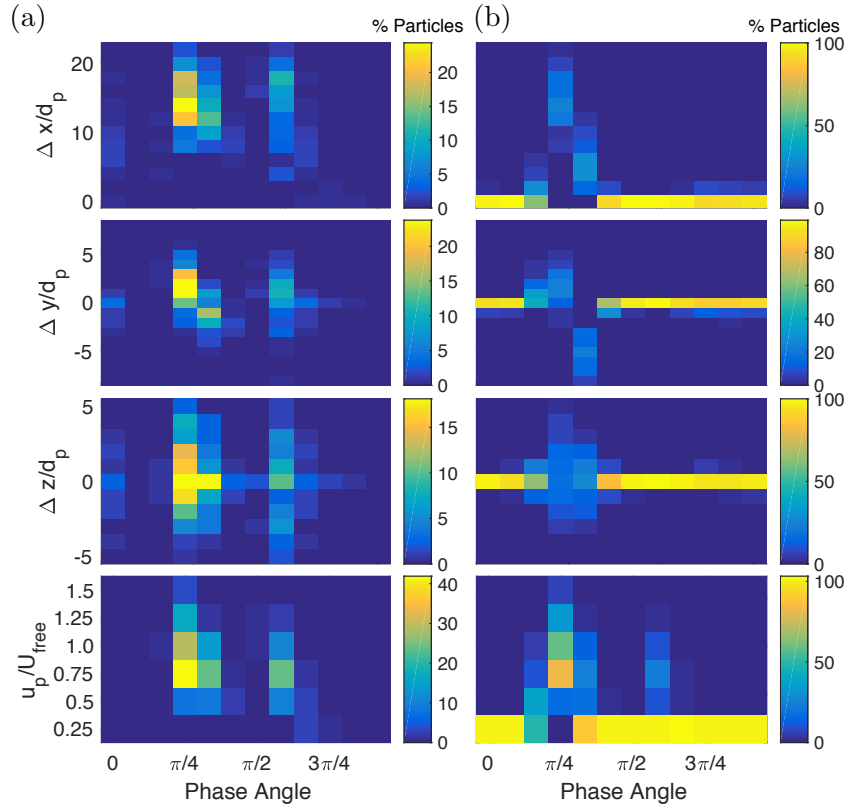


Figure 16: Suspended particle displacements and velocities, shown as distributions of total suspended particles. (a) The four figures on the left describe the behavior of particles determined to be suspended at the indicated phase times shown on the x-axis. (b) The four figures on the right show the full history of the particles determined to be suspended at phase time $\frac{\pi}{4}$ only. Thus, the four figures on the right show a distinct peak of displacement and velocity around phase time $\frac{\pi}{4}$, which mostly drops off before and after $\frac{\pi}{4}$.

5.8 Bed Load

In this work, suspended particles (discussed in Section 5.7) are defined to be “suspended” if they are found to be above the fluid-bed interface, as defined in Section 5.5. However, these are not the only particles in motion, as there is a mobile layer of particles at the fluid-bed interface, known as “bed load”. As noted by Durán et. al. [21], a transport layer forms in beds under unidirectional flow. In the oscillatory system presented in this work, this transport layer is isolated to the ripple peaks and faces. Below the fluid-bed interface of Figure 12, the mobile transport layer consists of particles rolling and sliding, also known as reptation. The layer is thickest at the ripple peak, and tapers down the ripple faces.

The particles in the transport layer are grouped into three modes based on their initial and final positions over the course of a half oscillation period: (1) particles that remain on the upstream side of the ripple peak; (2) particles that remain on the downstream side of the ripple peak; and (3) particles that are mobilized from the upstream side to the downstream side of the ripple peak. For brevity, particles in groups 1, 2, and 3 will be referred to as “upstream”, “downstream”, and “traverse” particles. The normalized particle pathways of each mode are shown in Figure 17. The initial particle positions have been normalized in the spanwise direction such that $z = 0$ for all particles. Within each mode, there is a range of motion, but the transport layer thickness is consistently $4d_p - 5d_p$ at the ripple peak for all modes. Traverse particles also include the saltating particles described in Section 5.7, but these make up a small proportion of the total particles in motion.

Figure 18 presents the mean pathways and the corresponding single standard deviation range of each mode. Upstream and downstream mean pathways are roughly extensions of the transverse mean pathway, though not exactly. The downstream particles are not subject to the same shear stress as those on the upstream ripple face, so the magnitude of their motion is smaller than the upstream particles. As the first row of Figure 18 shows, the mean pathway of all particles in the transport layer essentially mirrors that of the transverse particles, indicating that the dominant mode of motion is the traversing movement from the upstream side to the downstream side of the ripple peak. At phase time $\frac{\pi}{4}$, although the shapes of these two mean pathways are similar, the locations of the pathway zeniths are different. The peak of the total mean transport layer pathway is roughly $(x, y) = (-3, 21)d_p$, and the peak of the mean traverse particle pathway is $(x, y) = (-2, 22)d_p$. Keeping in mind that the ripple peak itself is roughly $(x, y) = (-3, 24)d_p$ (skewed to the left of the origin), as shown in Figure 11, these particles must be moving below the fluid-bed interface. By comparison, the peak of the saltating particles is roughly $(x, y) = (6, 24)d_p$, which is well above the the fluid-bed interface, as expected.

Since the dominant mode of motion is from the upstream side to the downstream side of the ripple peak, the particles are not separated by mode to examine their spatial displacements and velocity. Maximum particle displacement and velocity is observed at the time of maximum fluid acceleration, phase time $\frac{\pi}{4}$, in Figure 19. As expected, the magnitudes of the average streamwise bed load displacements and velocities are significantly less than in the suspended load regime. The positive-then-negative displacement in the wall-normal direction is reflected in the motion of the transport layer, but of course, much less dramatically than the saltating particles. The general trends in the bed load are seen as well in the suspended load, in all directions, but at a smaller scale. Suspended particles exhibit a peak velocity of $u_p/U_{free} \simeq 1$, where the particles in the transport layer show a maximum at just $u_p/U_{free} \leq 0.25$.

Here, again, the four left figures show displacement and velocity for any particle that is defined as in motion at the indicated phase time *only*. The four figures on the right show the evolution of particles that are deemed to be in motion at phase time $\frac{\pi}{4}$ only. These figures show a peak in displacement and velocity at $\frac{\pi}{4}$ and a drop to essentially no motion and zero particle velocity for the remainder of the half oscillation period. On the other hand, since the four figures on the left can (and do) contain different particles at each phase time, two different peaks in motion/velocity are observed. As noted in Section 5.7, due to the impact of

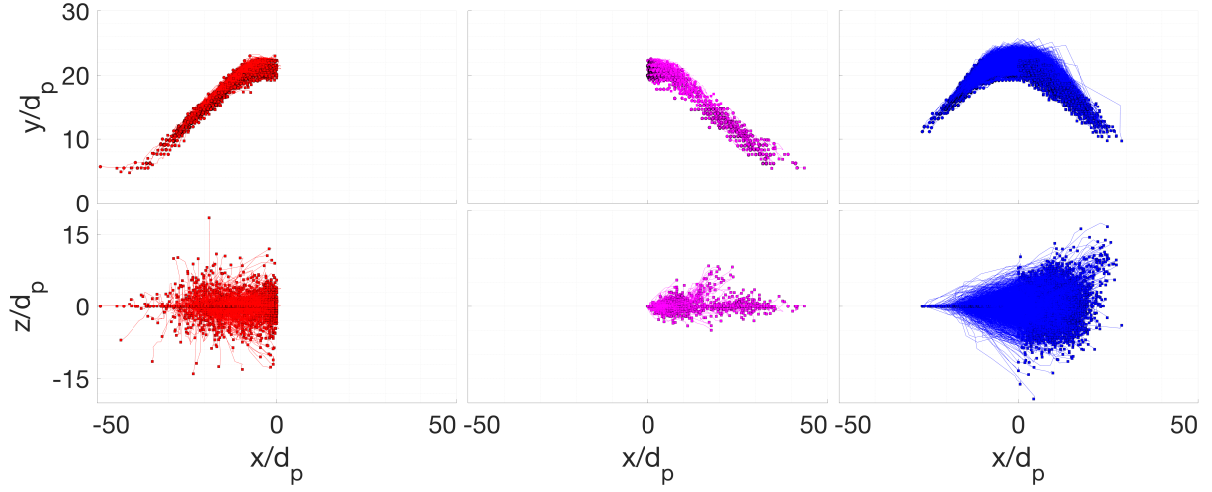


Figure 17: Normalized bed load particle pathways over a single half oscillation period, at phase time $\frac{\pi}{4}$. Pathways have been normalized for an initial z -position of 0. The first, second, and third columns show the pathways of the upstream, downstream, and traversing particles, respectively. Particle positions at phase times 0 and π are denoted by circles and squares, respectively.

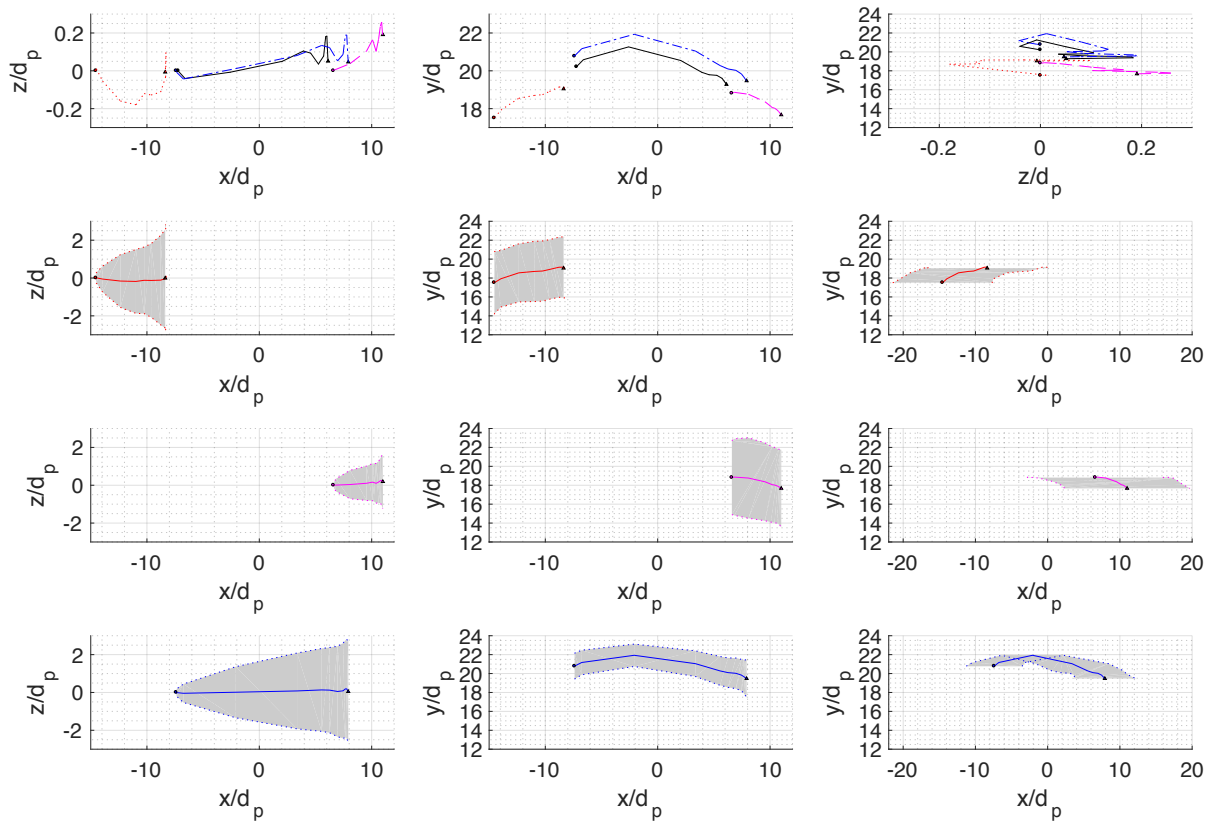


Figure 18: First row shows the mean particle pathways of upstream (red dotted line), downstream (magenta dashed line), traversing particles (blue dash-dot line), and all particles (black solid line). The second, third, and fourth rows shows the mean and shaded single standard deviations of the upstream, downstream, and traversing particles, respectively.

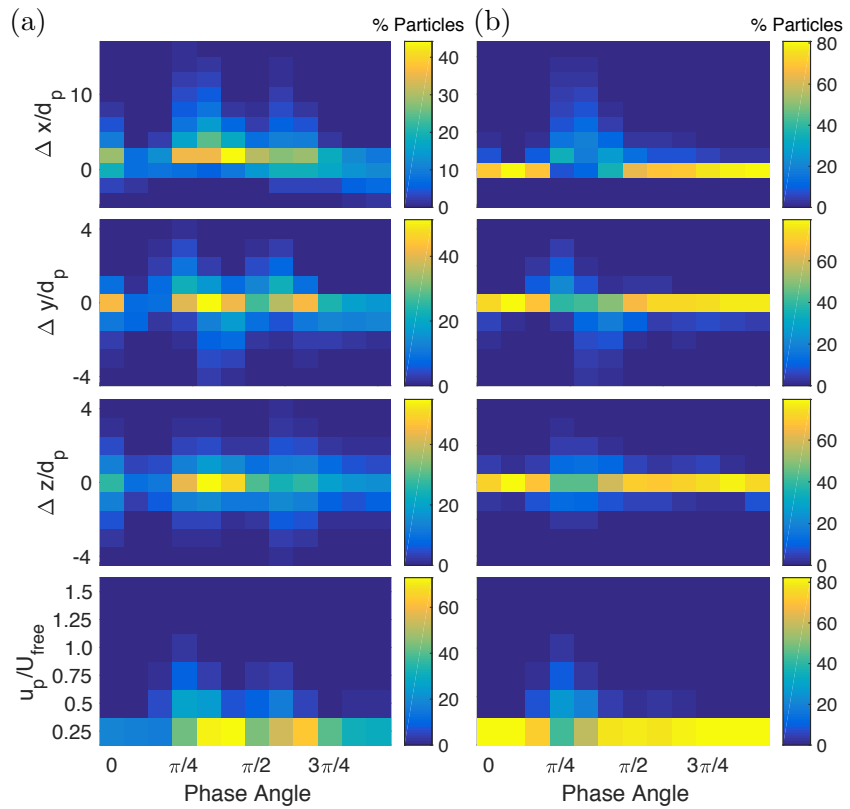


Figure 19: Bed load particle displacements and velocities, shown as distributions of total bed load particles. (a) The four left figures describe the behavior of particles determined to be in the bed load regime at the indicated phase times shown on the x-axis. (b) The four figures on the right show the full history of the particles determined to be in the bed load regime at phase time $\frac{\pi}{4}$ only. Thus, the four figures on the right show a distinct peak of displacement and velocity around phase time $\frac{\pi}{4}$, which mostly drops off before and after $\frac{\pi}{4}$.

the shear layer shed from the adjacent upstream ripple, two maximums in particle displacement and velocity are observed. The absolute maximum momentum transfer occurs at phase time $\frac{\pi}{4}$, and the second weaker wave of momentum transfer occurs just after the peak freestream velocity is achieved, around phase time $\frac{7\pi}{12}$.

The particle displacements and velocities shown in Figure 19 are illustrated in another way in Figure 20. Over the spanwise width of a single ripple, all particles in motion (bed load and suspended load) are binned by their streamwise position on the wavelength of the ripple. The number of particles in these bins are plotted as circles, at their locations along the wavelength of the ripple. The magnitude of the circle diameter is proportional to the number of particles in that bin. Additionally, the circles are colored by the average particle velocity of the particles in that bin. This is done over a half period of oscillation to understand the evolution of the location, and direction, of particle motion. As expected, at phase times $\frac{3\pi}{12}$, $\frac{4\pi}{12}$ and $\frac{5\pi}{12}$, the bulk of the particles in motion are found at the the top, or slightly upstream side, of the ripple peak, and the average particle velocity is from left-to-right, the same direction as the freestream fluid velocity. At these phase times, there is hardly any particle motion anywhere besides the ripple peak. As can be seen at phase time $\frac{4\pi}{12}$, almost zero particle motion is observed beyond $\pm 20d_p$ of the ripple peak centerline. Interestingly, at phase times before and after maximum particle motion, particle velocities opposite the freestream fluid velocity are observed along the lower parts of the ripple faces. At phase time 0, there is minimal particle motion around the ripple peak, but there are greater concentrations of particle motion around $-30d_p$ and $+15d_p$ from the ripple peak. It is this interplay of opposite-direction particle motion at the ripple peaks and faces, due to turbulent structures churning between ripples as the flow reverses direction, that maintains the ripple structure in a quasi-equilibrium state.

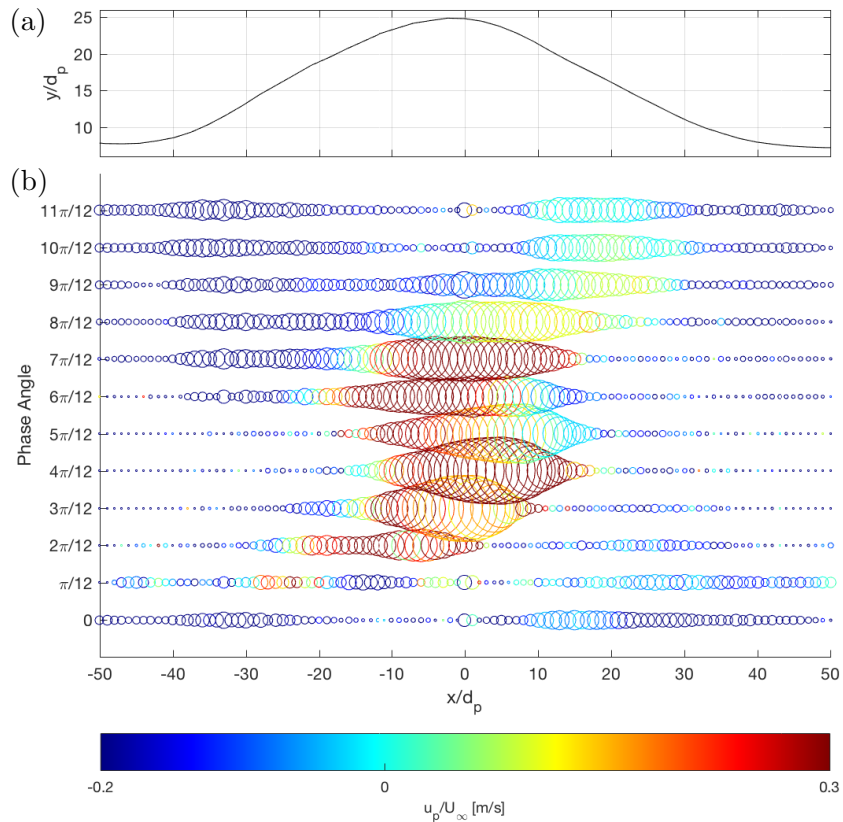


Figure 20: (a) The typical ripple profile shape, and (b) a scatter plot where the magnitude of the circle diameter reflects the amount of particles in motion at that location of the ripple (i.e. a larger circle indicates a location of greater particle motion), at the indicated phase time. The scatter plot circles are colored by the normalized average streamwise particle velocity, u_p/U_∞ .

5.9 Solid-Fluid Interaction

Figures 21 and 22 show a bottom-up (in the positive y direction) perspective of the evolution of particle motion pathways and fluid coherent structures in the fluid. The evolution is shown over a half oscillation period at phase times $\frac{n\pi}{12}$ for $n = 0, \dots, 12$. Figure 21 shows the accelerative first quarter of the oscillation period, or phase times $\frac{n\pi}{12}$ for $n = 0, \dots, 6$. Figure 22 shows the decelerative second quarter of the oscillation period, or phase times $\frac{n\pi}{12}$ for $n = 6, \dots, 12$. It is important to note that both figures show phase time $\frac{6\pi}{12}$ in order to provide continuity between the two figures. In both figures, the top panel shows the spanwise average ripple profile, and the remaining panels show the evolution of the solid-fluid interaction. The pathways of particles in motion are displayed as lines, with different colors for every particle. The coherent structures of the fluid, determined by the Q-criterion, are colored by the *spanwise* fluid velocity. Intuitively, as the fluid velocity increases, more particles are in motion, mostly moving in parallel to the bulk fluid motion in the streamwise direction. However, as the fluid accelerates and streamwise vortices are formed on the upstream faces of the ripples, they occasionally form counter-rotating pairs, allusive the well known observation of Görtler vortices forming on concave walls (Saric [40], Tseng and Ferziger [47]). This phenomenon occurs at various scales, but two of the larger scale occurrences are circled at phase time $\frac{6\pi}{12}$, when the pairings first occur.

Two different types of streamwise vortex pairings occur. One type pulls particles toward the vortex pair centerline, and the other pulls them away from the centerline. In this work, these are designated as “pinching” and “bursting” vortex pairs, respectively. Since Figures 21 and 22 are bottom-up views, the “underside” of the vortices are what is seen. This reflects the sides of the vortices which are closest to, and thus interact with, the rippled bed. Looking at phase time $\frac{6\pi}{12}$, one of each type of vortex pair is circled. The pinching pair centered at $x/d_p \simeq -225$ has tangential velocities on their undersides which are directed towards each other. This vortex pair pinches particles toward the vortex pair centerline, as seen in Figure 22. The bursting pair at centered at $x/d_p \simeq 175$ displays tangential velocities on their undersides directed in opposite directions. This vortex pair pulls particles away from the vortex pair centerline in a bursting pattern, and the particles generally experience a greater displacement than those propeled by a pinching vortex pair. The effect of these vortex pairs on the particle motion is in line with the observations of 2D and 3D sediment behavior by Zedler and Street [51] [52], Scandura et al. [41], and Chang and Scotti [10].

In order to quantify the relationship between the fluid and solid phases, Figure 23 shows the TKE, calculated at the locations of the particles in motion, as a function of the amount of bed load and suspended load. Over a half oscillation period, the TKE was calculated at the location of every particle found to be in motion. The total number of particles with the same TKE values were then summed up. These summations were done separately for particles in the bed load and suspended load regimes. As expected, the suspended load did not experience the lower range of TKE values. However, the bed load and suspended load experienced similar TKE values at the high end of the range. But the shapes of the curves do indicate that, on average, the bed load (with a mode value ~ 0.5) experienced much lower TKE values than the suspended load (with a mode value ~ 1.5).

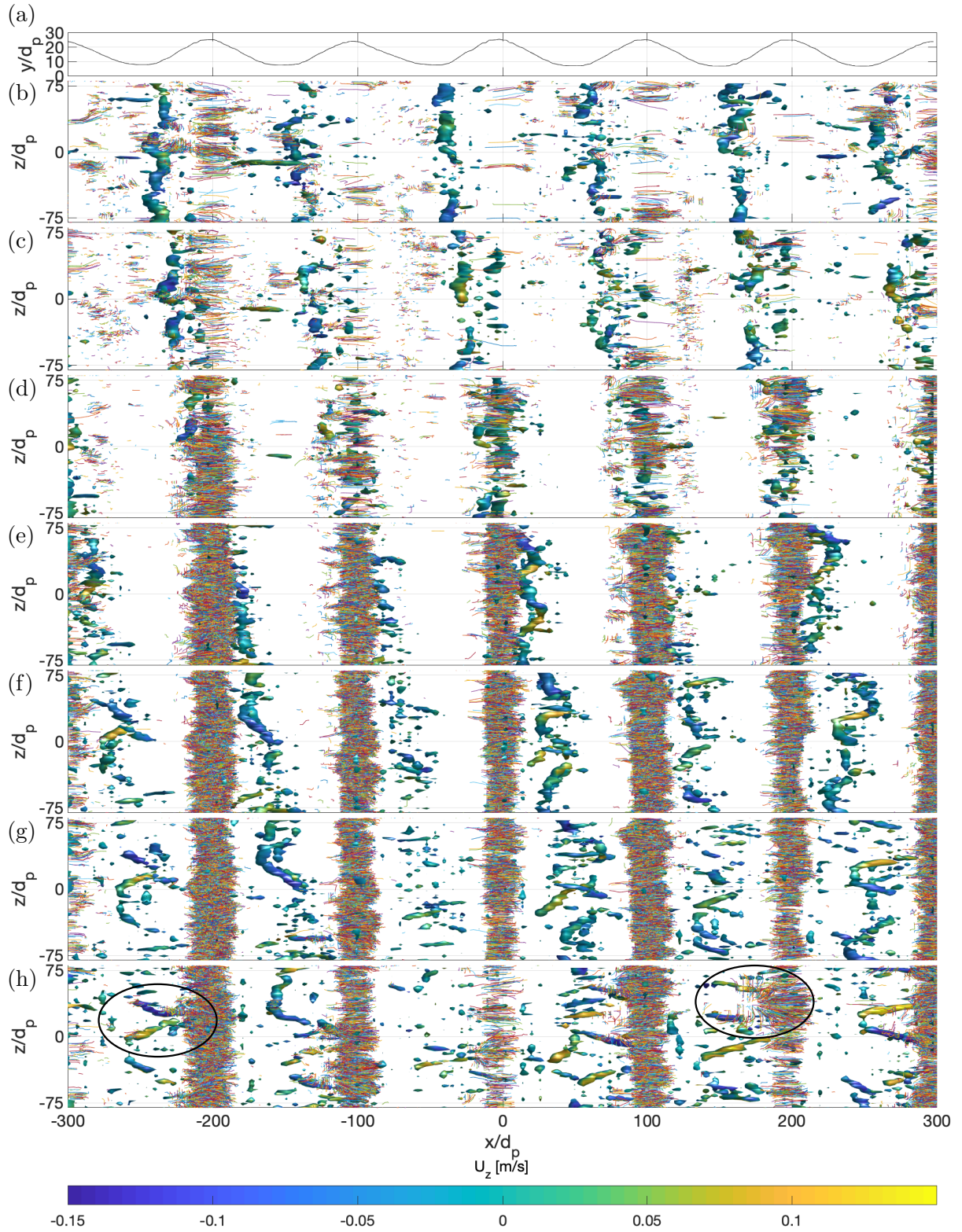


Figure 21: Particle pathways and fluid coherent structures. (a) Spanwise average ripple profile. (b)-(h) Bottom-up (positive y -direction perspective) view of particle pathways denoted by colored lines, and fluid coherent structures visualized by the Q-criterion, colored by spanwise fluid velocity. All dimensions are normalized by particle diameter. Phase times: (b) $\frac{0\pi}{12}$, (c) $\frac{1\pi}{12}$, (d) $\frac{2\pi}{12}$, (e) $\frac{3\pi}{12}$, (f) $\frac{4\pi}{12}$, (g) $\frac{5\pi}{12}$, and (h) $\frac{6\pi}{12}$, repeated in Figure 22(b) for continuity.

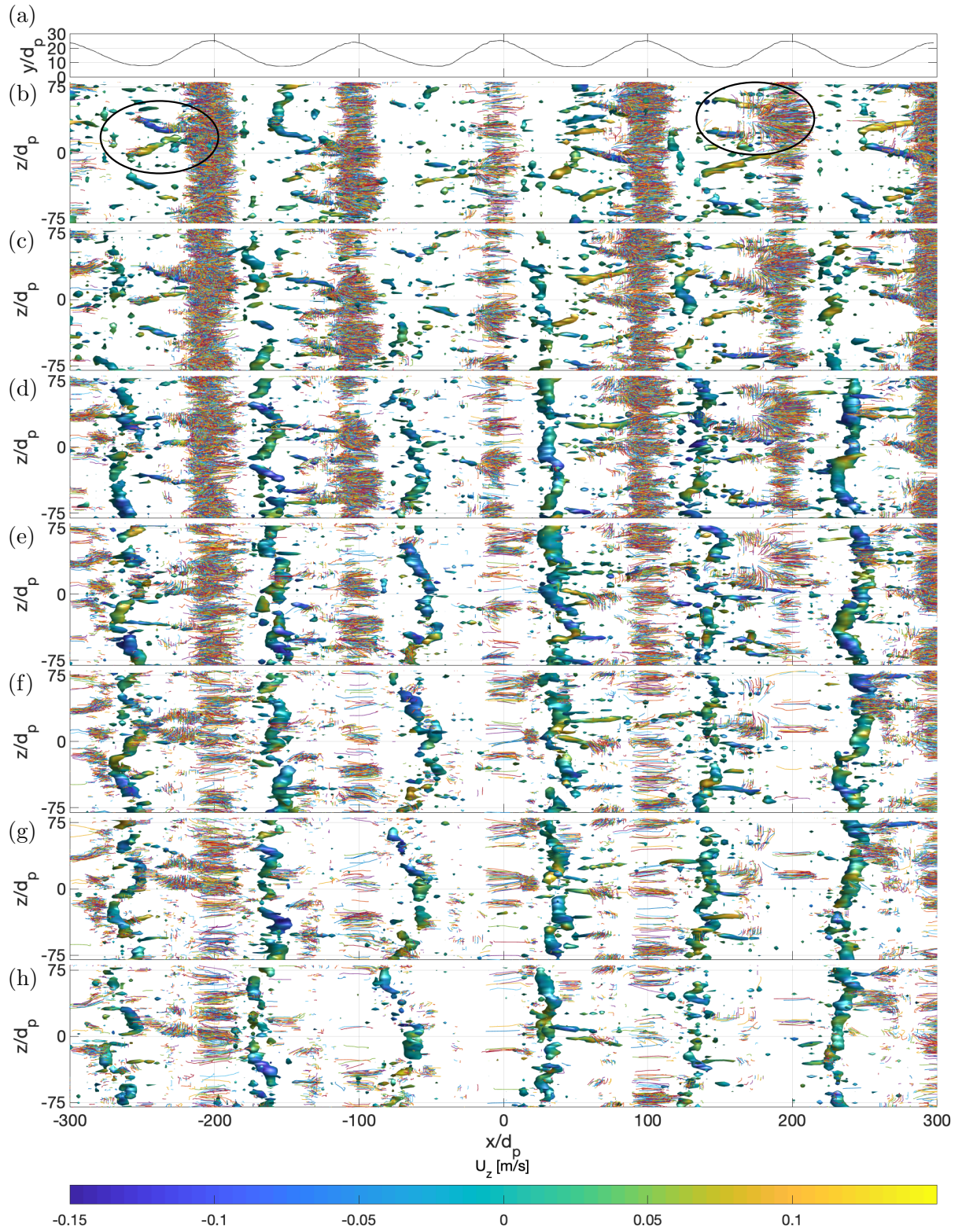


Figure 22: Particle pathways and fluid coherent structures. (a) Spanwise average ripple profile. (b)-(h) Bottom-up (positive y -direction perspective) view of particle pathways denoted by colored lines, and fluid coherent structures visualized by the Q-criterion, colored by spanwise fluid velocity. All dimensions are normalized by particle diameter. Phase times: (b) $\frac{6\pi}{12}$, repeated in Figure 21(h) for continuity, (c) $\frac{7\pi}{12}$, (d) $\frac{8\pi}{12}$, (e) $\frac{9\pi}{12}$, (f) $\frac{10\pi}{12}$, (g) $\frac{11\pi}{12}$, and (h) $\frac{12\pi}{12}$.

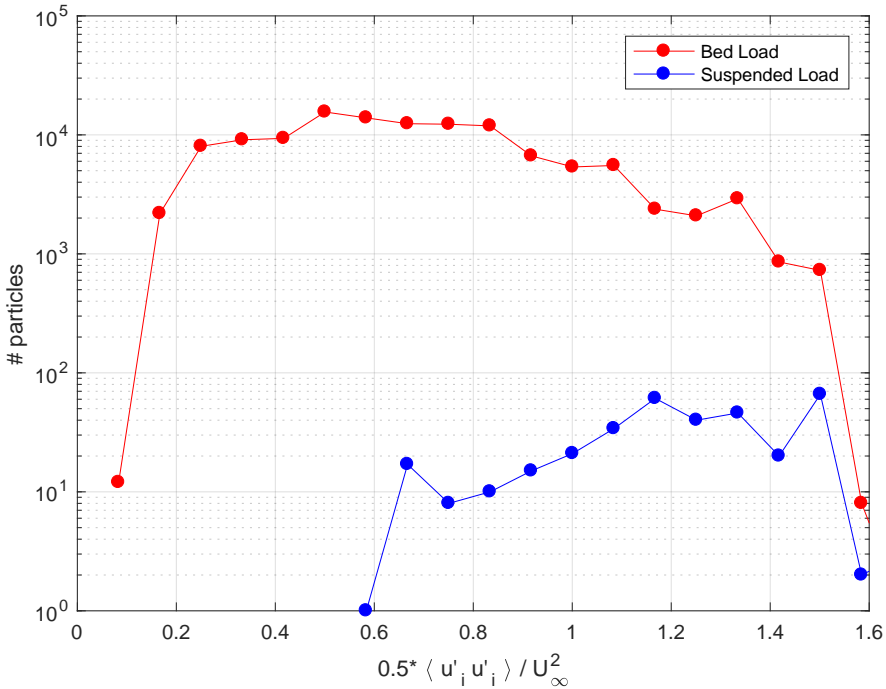


Figure 23: The fluid TKE is calculated at the locations of the particles in motion, then the total number of particles at a given TKE value are summed up over a half oscillation period. Naturally, suspended particles tended towards higher TKE values, but the bed load experienced similarly high TKE values overall.

6 Conclusion

This work investigates the evolution of a sinusoidally rippled particle bed under the effect of an oscillatory flow. A Large-Eddy Simulation (LES) was conducted to approximate the conditions of an experiment conducted in the small-oscillatory flow tunnel at the Sediment Dynamics Laboratory of the Naval Research Laboratory, Stennis Space Center, MS. The simulation uses the Discrete Particle Method (DPM), which is an Euler-Lagrange approach, where particles and fluid are four-way coupled.

In the experimental work, a closed channel of water, over an initially flat sand bed, is driven to oscillatory flow. Eventually, the system reaches a quasi-equilibrium in which spanwise oriented ripples have formed in the sand bed. The ripples are roughly sinusoidal in shape, with a wavelength roughly five times the amplitude. Stereographic PIV data captured fluid velocity in a two-dimensional plane around a single ripple for eleven oscillation periods. The LES was configured to approximate the configuration of this steady-state in the oscillatory flow channel by prescribing a sinusoidal ripple morphology and driving the flow by a cosinusoidal pressure gradient. The three-dimensional domain contains six ripples and the fluid was initially at rest. The flow is then driven by the cosinusoidal pressure gradient and the system requires three full periods for the bed shear stress to converge. In both the experimental work and the LES, as the flow accelerates, a shear layer forms at the stoss side of the ripple. As the flow achieves its maximum freestream velocity and begins to decelerate, the shear layer forms a spanwise vortex which detaches from the ripple peak on the lee side. When the flow has decelerated back to zero in the freestream, the halfway point of the oscillation period, this vortex is detached between ripples. As the flow is accelerated in the opposite direction, this detached vortex is shed into the freestream as another shear layer is formed at the ripple peak, and the whole process is mirrored in the second half of the oscillation period.

This work shows the viability of the LES-DPM methodology to reproduce the mesoscale features of a quasi-steady-state rippled bed under oscillatory flow conditions. Based on wall-normal profiles of velocity and the turbulent kinetic energy budget, along with velocity streamlines and vorticity, the LES proves capable of capturing the mesoscale features of the experimental flow. Reproduction of Görtler-like streamwise vortex pairings, well-known to form on concave walls, was also observed. These vortex pairings produced strong spanwise particle motion, either in a pinching or bursting pattern, on the upstream ripple faces.

Additionally, the DPM is able to provide some insight into the complex erosive processes at the individual particle scale. Particle motion is observed to take place by saltation at the top most layers of the fluid-bed interface and by reptation within a transport layer at the ripple peaks and upper parts of the ripple faces. The behavior is coupled to the three-dimensional nature of the coherent structures in the oscillatory flow. It is observed that the bulk of the erosive processes occur at the time of maximum fluid acceleration, phase time $\frac{\pi}{4}$, but a second, smaller, peak in particle displacement and velocity is observed at phase time $\frac{7\pi}{12}$, just after the fluid achieves the maximum freestream velocity. This is due to the direct interaction of fluid structures shed from adjacent ripple peaks, and the unsteady, wavy shape of the spanwise vortices shed from the ripple peak, manifested as non-uniform shear layers at the upstream ripple faces. Thus, the intensity of the shear layer displays spatial and temporal variation, resulting in two peaks in particle motion. In both cases, the coupling between the fluid and solid phases maintains the ripple structure and the quasi-equilibrium state of the system.

References

- [1] AKHAVAN, R., KAMM, R., AND SHAPIRO, A. An investigation of transition to turbulence in bounded oscillatory stokes flows part 2. numerical simulations. *Journal of fluid mechanics* 225 (1991), 423–444.
- [2] AROLLA, S. K., AND DESJARDINS, O. Transport modeling of sedimenting particles in a turbulent pipe flow using euler–lagrange large eddy simulation. *International Journal of Multiphase Flow* 75 (2015), 1–11.
- [3] BAGNOLD, R. A., AND TAYLOR, G. Motion of waves in shallow water. interaction between waves and sand bottoms. In *Proceedings of the Royal Society of London A: Mathematical, Physical and Engineering Sciences* (1946), vol. 187, The Royal Society, pp. 1–18.
- [4] BENJAMIN, T. B. Shearing flow over a wavy boundary. *Journal of Fluid Mechanics* 6, 2 (1959), 161–205.
- [5] BEST, J. The fluid dynamics of river dunes: A review and some future research directions. *Journal of Geophysical Research: Earth Surface* 110, F4 (2005).
- [6] BLONDEAUX, P. Sand ripples under sea waves part 1. ripple formation. *Journal of Fluid Mechanics* 218 (1990), 1–17.
- [7] CAPECELATRO, J., AND DESJARDINS, O. An euler–lagrange strategy for simulating particle-laden flows. *Journal of Computational Physics* 238 (2013), 1–31.
- [8] CAPECELATRO, J., AND DESJARDINS, O. An euler–lagrange strategy for simulating particle-laden flows. *Journal of Computational Physics* 238 (2013), 1–31.
- [9] CAPECELATRO, J., AND DESJARDINS, O. Eulerian–lagrangian modeling of turbulent liquid–solid slurries in horizontal pipes. *International journal of multiphase flow* 55 (2013), 64–79.

- [10] CHANG, Y. S., AND SCOTTI, A. Entrainment and suspension of sediments into a turbulent flow over ripples. *Journal of turbulence* 4, 19 (2003), 1–22.
- [11] CHARRU, F., ANDREOTTI, B., AND CLAUDIN, P. Sand ripples and dunes. *Annual Review of Fluid Mechanics* 45 (2013), 469–493.
- [12] CHARRU, F., AND HINCH, E. Ripple formation on a particle bed sheared by a viscous liquid. part 1. steady flow. *Journal of Fluid Mechanics* 550 (2006), 111–121.
- [13] CHARRU, F., AND HINCH, E. Ripple formation on a particle bed sheared by a viscous liquid. part 2. oscillating flow. *Journal of Fluid Mechanics* 550 (2006), 123–137.
- [14] CHONG, M. S., PERRY, A. E., AND CANTWELL, B. J. A general classification of three-dimensional flow fields. *Physics of Fluids A: Fluid Dynamics* 2, 5 (1990), 765–777.
- [15] CHURCH, M. Bed material transport and the morphology of alluvial river channels. *Annu. Rev. Earth Planet. Sci.* 34 (2006), 325–354.
- [16] CUNDALL, P. A., AND STRACK, O. D. A discrete numerical model for granular assemblies. *Geotechnique* 29, 1 (1979), 47–65.
- [17] DEEN, N., VAN SINT ANNALAND, M., VAN DER HOEF, M., AND KUIPERS, J. Review of discrete particle modeling of fluidized beds. *Chemical Engineering Science* 62, 1 (2007), 28–44.
- [18] DERKSEN, J. J. Simulations of granular bed erosion due to a mildly turbulent shear flow. *Journal of Hydraulic Research* 53, 5 (2015), 622–632.
- [19] DESJARDINS, O., BLANQUART, G., BALARAC, G., AND PITSCHE, H. High order conservative finite difference scheme for variable density low mach number turbulent flows. *Journal of Computational Physics* 227, 15 (2008), 7125–7159.
- [20] DI LIBERTO, M., AND CIOFALO, M. Numerical simulation of reciprocating turbulent flow in a plane channel. *Physics of fluids* 21, 9 (2009), 095106.
- [21] DURÁN, O., ANDREOTTI, B., AND CLAUDIN, P. Numerical simulation of turbulent sediment transport, from bed load to saltation. *Physics of Fluids* 24, 10 (2012), 103306.
- [22] ENGELUND, F., AND FREDSOE, J. Sediment ripples and dunes. *Annual Review of Fluid Mechanics* 14, 1 (1982), 13–37.
- [23] FORNARELLI, F., AND VITTORI, G. Oscillatory boundary layer close to a rough wall. *European Journal of Mechanics-B/Fluids* 28, 2 (2009), 283–295.
- [24] FRANK, D., FOSTER, D., SOU, I. M., AND CALANTONI, J. Incipient motion of surf zone sediments. *Journal of Geophysical Research: Oceans* 120, 8 (2015), 5710–5734.
- [25] FRANK, D., FOSTER, D., SOU, I. M., CALANTONI, J., AND CHOU, P. Lagrangian measurements of incipient motion in oscillatory flows. *Journal of Geophysical Research: Oceans* 120, 1 (2015), 244–256.
- [26] FRANK-GILCHRIST, D. P., PENKO, A., AND CALANTONI, J. Investigation of sand ripple dynamics with combined particle image and tracking velocimetry. *Journal of Atmospheric and Oceanic Technology* 35, 10 (2018), 2019–2036.
- [27] GERMANO, M., PIOMELLI, U., MOIN, P., AND CABOT, W. H. A dynamic subgrid-scale eddy viscosity model. *Physics of Fluids A: Fluid Dynamics* 3, 7 (1991), 1760–1765.

- [28] GHODEK, C. D., AND APTE, S. V. Dns study of particle-bed–turbulence interactions in an oscillatory wall-bounded flow. *Journal of Fluid Mechanics* 792 (2016), 232–251.
- [29] GUNDOGDU, M. Y., AND CARPINLIOGLU, M. O. Present state of art on pulsatile flow theory: Part 1: Laminar and transitional flow regimes. *JSME International Journal Series B Fluids and Thermal Engineering* 42, 3 (1999), 384–397.
- [30] GUNDOGDU, M. Y., AND CARPINLIOGLU, M. O. Present state of art on pulsatile flow theory: Part 2: Turbulent flow regime. *JSME International Journal Series B Fluids and Thermal Engineering* 42, 3 (1999), 398–410.
- [31] HINO, M., KASHIWAYANAGI, M., NAKAYAMA, A., AND HARA, T. Experiments on the turbulence statistics and the structure of a reciprocating oscillatory flow. *Journal of Fluid Mechanics* 131 (1983), 363–400.
- [32] HINO, M., SAWAMOTO, M., AND TAKASU, S. Experiments on transition to turbulence in an oscillatory pipe flow. *Journal of Fluid Mechanics* 75, 2 (1976), 193–207.
- [33] KIDANEMARIAM, A. G., AND UHLMANN, M. Direct numerical simulation of pattern formation in subaqueous sediment. *Journal of Fluid Mechanics* 750 (2014).
- [34] KIDANEMARIAM, A. G., AND UHLMANN, M. Formation of sediment patterns in channel flow: minimal unstable systems and their temporal evolution. *Journal of Fluid Mechanics* 818 (2017), 716–743.
- [35] LILLY, D. K. A proposed modification of the germano subgrid-scale closure method. *Physics of Fluids A: Fluid Dynamics* 4, 3 (1992), 633–635.
- [36] MAZZUOLI, M., KIDANEMARIAM, A. G., BLONDEAUX, P., VITTORI, G., AND UHLMANN, M. On the formation of sediment chains in an oscillatory boundary layer. *Journal of Fluid Mechanics* 789 (2016), 461–480.
- [37] MENEVEAU, C., LUND, T. S., AND CABOT, W. H. A lagrangian dynamic subgrid-scale model of turbulence. *Journal of Fluid Mechanics* 319 (1996), 353–385.
- [38] PAOLA, C., AND VOLLE, V. A generalized exner equation for sediment mass balance. *Journal of Geophysical Research: Earth Surface* 110, F4 (2005).
- [39] PEPIOT, P., AND DESJARDINS, O. Numerical analysis of the dynamics of two-and three-dimensional fluidized bed reactors using an euler–lagrange approach. *Powder Technology* 220 (2012), 104–121.
- [40] SARIC, W. S. Görtler vortices. *Annual Review of Fluid Mechanics* 26, 1 (1994), 379–409.
- [41] SCANDURA, P., VITTORI, G., AND BLONDEAUX, P. Three-dimensional oscillatory flow over steep ripples. *Journal of Fluid Mechanics* 412 (2000), 355–378.
- [42] SCHMEECKLE, M. W. Numerical simulation of turbulence and sediment transport of medium sand. *Journal of Geophysical Research: Earth Surface* 119, 6 (2014), 1240–1262.
- [43] SCOTTI, A., AND PIOMELLI, U. Numerical simulation of pulsating turbulent channel flow. *Physics of Fluids* 13, 5 (2001), 1367–1384.
- [44] SMAGORINSKY, J. General circulation experiments with the primitive equations: I. the basic experiment. *Monthly weather review* 91, 3 (1963), 99–164.
- [45] SUN, R., AND XIAO, H. Cfd–dem simulations of current-induced dune formation and morphological evolution. *Advances in Water Resources* 92 (2016), 228–239.

- [46] TENNETI, S., GARG, R., AND SUBRAMANIAM, S. Drag law for monodisperse gas–solid systems using particle-resolved direct numerical simulation of flow past fixed assemblies of spheres. *International journal of multiphase flow* 37, 9 (2011), 1072–1092.
- [47] TSENG, Y.-H., AND FERZIGER, J. H. Large-eddy simulation of turbulent wavy boundary flow—illustration of vortex dynamics. *Journal of turbulence* 5, 34 (2004), 1–23.
- [48] VITTORI, G., AND BLONDEAUX, P. Sand ripples under sea waves part 2. finite-amplitude development. *Journal of Fluid Mechanics* 218 (1990), 19–39.
- [49] VITTORI, G., AND VERZICCO, R. Direct simulation of transition in an oscillatory boundary layer. *Journal of Fluid Mechanics* 371 (1998), 207–232.
- [50] YALIN, M. S. *Mechanics of Sediment Transport: 2d Ed.* Pergamon Press, 1977.
- [51] ZEDLER, E. A., AND STREET, R. L. Large-eddy simulation of sediment transport: currents over ripples. *Journal of Hydraulic Engineering* 127, 6 (2001), 444–452.
- [52] ZEDLER, E. A., AND STREET, R. L. Sediment transport over ripples in oscillatory flow. *Journal of Hydraulic Engineering* 132, 2 (2006), 180–193.
- [53] ZHU, H., ZHOU, Z., YANG, R., AND YU, A. Discrete particle simulation of particulate systems: theoretical developments. *Chemical Engineering Science* 62, 13 (2007), 3378–3396.
- [54] ZHU, H., ZHOU, Z., YANG, R., AND YU, A. Discrete particle simulation of particulate systems: A review of major applications and findings. *Chemical Engineering Science* 63, 23 (2008), 5728–5770.